

Prompt, early, and afterglow optical observations of five gamma-ray bursts (GRBs 100901A, 100902A, 100905A, 100906A, and 101020A)

E. S. Gorbovskoy^{1*}, G. V. Lipunova^{1†}, V. M. Lipunov¹, V. G. Kornilov¹,
 A. A. Belinski¹, N. I. Shatskiy¹, N. V. Tyurina¹, D. A. Kuvshinov¹,
 P. V. Balanutsa¹, V. V. Chazov¹, A. Kuznetsov¹, D. S. Zimnukhov¹,
 M. V. Kornilov¹, A. V. Sankovich¹, A. Krylov¹, K. I. Ivanov², O. Chvalaev²,
 V. A. Poleschuk², E. N. Konstantinov², O. A. Gress², S. A. Yazev², N. M. Budnev²,
 V. V. Krushinski³, I. S. Zalozhnych³, A. A. Popov³, A. G. Tlatov⁴,
 A. V. Parhomenko⁴, D. V. Dormidontov⁴, V. Sennik⁴, V. V. Yurkov⁵,
 Yu. P. Sergienko⁵, D. Varda⁵, I. P. Kudelina⁵, A. J. Castro–Tirado⁶,
 J. Gorosabel⁶, R. Sánchez–Ramírez⁶, M. Jelinek⁶, J. C. Tello⁶

¹*Sternberg Astronomical Institute, Moscow State University, Universitetskij pr. 13, Moscow 119992, Russia*

²*Irkutsk State University, ul. Karla Marxa 1, Irkutsk 664003, Russia*

³*Kourovka Astronomical Observatory, Physical Department of Ural State University, pr. Lenina 51, Ekaterinburg 620083, Russia*

⁴*Kislovodsk Solar Station of the Pulkovo Observatory RAS, P.O.Box 45, ul. Gagarina 100, Kislovodsk 357700, Russia*

⁵*Blagoveschensk Educational State University, ul. Lenina 104, Amur Region, Blagoveschensk 675000, Russia*

⁶*Instituto de Astrofísica de Andalucía (IAA-CSIC), Glorieta de la Astronomía s/n, 18008 Granada, Spain*

Accepted 2011 November 13. Received 2011 November 02; in original form 2011 June 24

ABSTRACT

We present results of the prompt, early, and afterglow optical observations of five γ -ray bursts, GRBs 100901A, 100902A, 100905A, 100906A, and 101020A, made with the Mobile Astronomical System of Telescope-Robots in Russia (MASTER-II net), the 1.5-m telescope of Sierra-Nevada Observatory, and the 2.56-m Nordic Optical Telescope. For two sources, GRB 100901A and GRB 100906A, we detected optical counterparts and obtained light curves starting before cessation of γ -ray emission, at 113 s and 48 s after the trigger, respectively. Observations of GRB 100906A were conducted in two polarizing filters. Observations of the other three bursts gave the upper limits on the optical flux; their properties are briefly discussed. More detailed analysis of GRB 100901A and GRB 100906A supplemented by *Swift* data provides the following results and indicates a different origin of the prompt optical radiation in the two bursts. The light curves patterns and spectral distributions suggest a common production site of the prompt optical and high-energy emission in GRB 100901A. Results of spectral fits for GRB 100901A in the range from the optical to X-rays favor power-law energy distributions and a consistent value of the optical extinction in the host galaxy. GRB 100906A produced a smoothly peaking optical light curve suggesting that the prompt optical radiation in this GRB originated in a front shock. This is supported by a spectral analysis. We have found that the Amati and Ghirlanda relations are satisfied for GRB 100906A. An upper limit on the value of the optical extinction on the host of GRB 100906A is obtained.

Key words: telescopes – gamma-ray burst: individual: GRB 100901A, GRB 100902A, GRB 100905A, GRB 100906A, GRB 101020A – gamma-ray burst: general.

1 INTRODUCTION

Since 1997, when the optical radiation of γ -ray bursts (GRBs) was first detected, it is known that they are the most energetic events in the Universe (Kulkarni et al. 1998). Optical emission observed hours after a GRB is attributed to the so-called afterglow, which is the result of a shock propagating outward in the surrounding media (Meszaros & Rees 1997). Characteristics of such emission are defined mainly by conditions in the interstellar media and the amount of the released energy but depend weakly on details of the central burst.

The physics of GRBs and emission mechanisms are not completely understood. A further progress calls for more observational data and model analysis. An acknowledged model is that a GRB is a manifestation of a formation of a rotating black hole (or another compact relativistic object) in a course of the gravitational collapse. An engine works that converts energy of the collapse into emissions of different types, among which a high-energy γ -emission is produced for up to several tens of seconds. The afterglow emission is detected long afterwards, while the engine is still working or not, which is uncertain. In order to understand better the details of the process, it is necessary to observe the main event itself, at different wavebands, while the engine is at its most active stage.

However, to observe prompt optical emission is a challenge as a GRB usually lasts no more than several tens of seconds. Beginning with the prompt optical observations of GRBs in 1998 of Akerlof et al. (2000), successful prompt optical detections remain rare. Evidently, two approaches can be conceived: to observe extensive sky fields waiting for a GRB to occur or to use special robotic telescopes ready to point anywhere by an alert from an orbital γ -ray observatory—‘alert observations’ technique. The Mobile Astronomical System of Telescope-Robots in Russia (MASTER-II¹) use both techniques (Lipunov et al. 2010). The present paper is dedicated to the alert MASTER observations of five GRBs in Siberia, Ural, and North Caucasus.

Alert ground-based optical observations of GRBs are a new global physical experiment available since the last decade. It is made possible thanks to the implementation of the global Internet network, powerful personal computers, and fast optical CCD-receivers. The challenge is to accomplish quickly the four following steps as early as possible:

- (i) a GRB is detected by a γ -ray telescope on board of a spacecraft (*Swift* (Gehrels et al. 2004), *Fermi* (Atwood et al. 2009), *INTEGRAL* (Winkler et al. 2003), etc.)
- (ii) after on-board processing is finished, location of a GRB is sent to the Gamma-ray bursts Coordinates Network (GCN) at NASA. The first two steps take from 10 to 40 seconds.
- (iii) the burst position is then disseminated to ground-based robotic telescopes through the Internet network – in about 0.5 s.
- (iv) robotic telescopes are scheduled and pointed to the received positions, which takes from 7 to 40 s for moderate-size instruments (less than 0.5 m) and from several minutes

to hours for 2m- and larger instruments. Whereupon, imaging is made in optical and IR bands.

The first Russian robotic telescope MASTER (Mobile Astronomical System of Telescope-Robots) came into operation in 2002 near Moscow thanks to the private funding of Moscow association ‘Optics’². Construction of the all-Russia network MASTER began in 2008 (Lipunov et al. 2010). Presently, telescopes of the MASTER-net are located in observatories of Moscow State University (in Kislovodsk), Ural State University (in Kourvka), and Irkutsk State University (in Tunka near Baikal Lake) and the Blagoveschensk Pedagogical University (in Blagoveschensk region). These observatories span six time zones. Description of the MASTER II telescopes can be found in Kornilov et al. (2011).

In September and October 2010, the MASTER telescopes made five target observations of GRBs that triggered the *Swift* observatory: GRBs 100901A, 100902A, 100905A, 100906A, and 101020A. In the present paper, we report these observations and make an analysis for two long GRBs, whose counterparts were successfully detected. For one of them, GRB 100906A, we also use the data obtained with the 1.5-m telescope at Sierra-Nevada Observatory (OSN) and 2.56-m Nordic Optical Telescope (NOT).

We begin in Section 2 with a description of the observations. Reduction and analysis of the data obtained by MASTER are described in Section 3. Preparation of *Swift* light curves and spectra from the data available online is also described there. In Section 4 we turn to the results for GRBs 100901A and 100906A: the spectra before T_{90} , the late-time spectra and the estimates of the optical extinction in the host galaxies, the search of the jet break time on the GRB 100906A light curve after 10 000 s. In Section 5 we consider the arguments for different sites of the prompt optical emission in GRBs 100901A and 100906A. We also discuss their spectral evolution, and the spectral characteristics of other GRBs, for which optical counterparts were not detected. The applicability of the Amati and Ghirlanda relations to GRBs 100901A and 100906A is checked. We also mention the model of a two-step collapse for the long engine activity that can cause a bump on the X-ray and optical light curve of GRB 100901A. We summarize our results in Section 6.

Throughout this work, we adopt a standard Λ CDM cosmology with $H_0 = 70 \text{ km s}^{-1} \text{ Mpc}^{-1}$, $\Omega_m = 0.27$, and $\Omega_\Lambda = 0.73$. We define the flux density power-law temporal and spectral decay indices as $F_\nu \propto t^{-\alpha} \nu^{-\beta}$, and the photon index equals $\beta + 1$. All errors in the paper are 1σ uncertainties unless otherwise noted. All *Swift* data used to reproduce light curves and spectra were taken from the *Swift* Catalog³, the UK *Swift* data archive⁴ and the Burst Analyser website.⁵

2 OBSERVATIONS

Presently the MASTER II net consists of four identical, fast telescopes located at different sites in Russia (Lipunov et al.

¹ MASTER web site: <http://observ.pereplet.ru>

² <http://www.ochkarik.ru/master/>

³ http://heasarc.nasa.gov/docs/swift/archive/grb_table/

⁴ http://www.swift.ac.uk/swift_portal/

⁵ http://www.swift.ac.uk/burst_analyser/

Table 1. Photometry of GRB 100901A by MASTER: R , unfiltered W , I , and V . Times $t - T_0$ are the middle times of exposures, which are listed in the 2nd, 5th, 8th, and 11th column. Full table can be found online in the electronic issue.

$t - T_0$ (h)	Exp. (s)	R (mag)	$t - T_0$ (h)	Exp. (s)	W (mag)	$t - T_0$ (h)	Exp. (s)	I (mag)	$t - T_0$ (h)	Exp. (s)	V (mag)
4.1381	180	18.08 ± 0.45	0.0315	20	18.93 ± 2.00	5.4149	180	17.00 ± 0.09	0.3811	180	17.96 ± 0.19
4.3939	180	17.81 ± 0.17	0.0426	30	18.23 ± 0.80	5.4719	180	16.96 ± 0.09	0.5449	180	17.96 ± 0.19
4.4545	180	17.56 ± 0.11	0.0591	40	18.42 ± 0.80	5.5288	180	17.07 ± 0.10	0.6021	180	17.76 ± 0.17
4.5129	180	17.61 ± 0.10	0.0950	60	18.53 ± 0.70	5.5857	180	16.87 ± 0.08	5.5865	180	17.59 ± 0.11
4.5705	180	17.45 ± 0.08	0.1185	80	17.51 ± 0.25	5.6426	180	17.04 ± 0.09	5.6451	180	17.70 ± 0.12
4.6278	180	17.77 ± 0.10	0.1475	100	18.47 ± 0.50	5.6999	180	17.04 ± 0.09	7.1125	180	17.92 ± 0.18
4.6857	180	17.33 ± 0.07	0.1820	120	18.85 ± 0.70	5.7568	180	17.05 ± 0.09	7.1718	180	17.79 ± 0.15
4.7428	180	17.56 ± 0.09	0.2233	150	18.62 ± 0.60	5.8138	180	16.83 ± 0.07			
4.8000	180	17.45 ± 0.07	0.2732	180	17.94 ± 0.30	5.8706	180	16.81 ± 0.07			
4.8571	180	17.39 ± 0.07	0.3272	180	17.99 ± 0.30	5.9277	180	16.92 ± 0.07			

2010; Kornilov et al. 2011). Each telescope is a twin-tube instrument with the aperture of 0.4 m and the focal ratio $f/2.5$. Each telescope is equipped with the CCD camera $4 \times 4K$ AltaU-16M providing a field of view of 2×2 square degrees. A photometric unit provides a set of four filters, which can be placed in turn at the optical axis before the CCD camera. Depending on the long-term scientific task, the photometric units of the twin telescopes are supplied with three filters (any of the following: Johnson B , V , R , I , and white glass). The fourth position is occupied by polarization filters, oriented orthogonally in the two tubes. Polarization filters are positioned differently in the celestial coordinate system at the telescopes of the MASTER net.

Each observatory operates automatically. Waiting for an alert signal, MASTER II monitors the sky searching for possible optical transients. Swapping from the monitoring to alert observations of GRBs is accomplished by switching the filters, focusing, and pointing the telescope to the event coordinates received from the GCN. In 20 seconds after an alert, the MASTER II observatory is ready to observe a GRB. The pointings at the positions of the GRBs considered below took from 22 to 47 s.

2.1 Prompt optical observations of GRB 100901A

GRB 100901A triggered the *Swift* Burst Alert Telescope (*Swift*/BAT) at 13:34:10 UT on September 1, 2010. Time T_{90} , during which 90 per cent of γ -fluence is detected, was 439 ± 33 s (Immler et al. 2010; Sakamoto et al. 2010b).

Two MASTER robotic telescopes were pointed to the *Swift* BAT position of GRB 100901A: at Tunka at 103 s after the BAT trigger time T_0 and near Blagoveschensk, 101 s after T_0 (Ivanov et al. 2010a). We have got more than ~ 5 min of optical observations simultaneous to the prompt γ -emission of the GRB. The source was too low above the horizon at Tunka, and it was possible to observe it with only one of the optical tubes. The second tube was shadowed by the dome, which made impossible measuring polarized light. The eastern telescope, near Blagoveschensk, was not operational because of the bad weather conditions. An optical flare, with maximum at 17.0^m in the MASTER unfiltered band, was clearly detected at 426 ± 40 s after the trigger time (Ivanov et al. 2010b), synchronously with the X-ray flare (Page & Immler 2010) and the γ -flare (Sakamoto et al. 2010b).

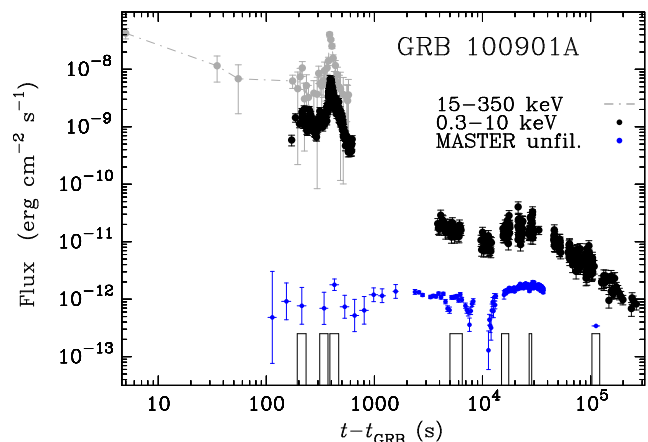


Figure 1. GRB 100901A optical light curve obtained by MASTER (blue points with vertical bars representing errors and horizontal bars representing exposure times; data are corrected for the Galactic extinction) along with the *Swift*/BAT 15-350 keV flux with 10 s binning (grey dots connected by dot-dashed lines) and *Swift*/XRT 0.3-10 keV unabsorbed flux (black dots; Page & Immler 2010). Thin-line rectangles show the time intervals selected for spectral analysis. Color figures can be viewed in the electronic version.

The MASTER telescope at Kourvka was pointed to GRB 100901A ~ 5 hours later. Overall, we have been continuously observing the GRB during 14 hours at three sites, Tunka, Kourvka, and Kislovodsk, in different optical bands: unfiltered, R , I , and V . The resulting data are summarized in Table 1 and presented in Figs. 1 and 2. In Fig. 1, *Swift*/XRT 0.3-10 keV and *Swift*/BAT 15-350 keV light curves for GRB 100901A are shown as well (for description see Section 3.3).

OSN observed the GRB about 11 hours after the trigger (Sanchez-Ramirez et al. 2010). The redshift of the host galaxy $z=1.408$ was obtained at the 8-m Gemini-North telescope (Chornock et al. 2010).

2.2 Prompt optical observations of GRB 100902A

On September the 2nd, the Kourvka MASTER telescope was pointed to the BAT position of GRB 100902A (Sakamoto et al. 2010c) 104 s after the GRB trigger time T_0 19:31:54 UT. This GRB flaring activity lasted for

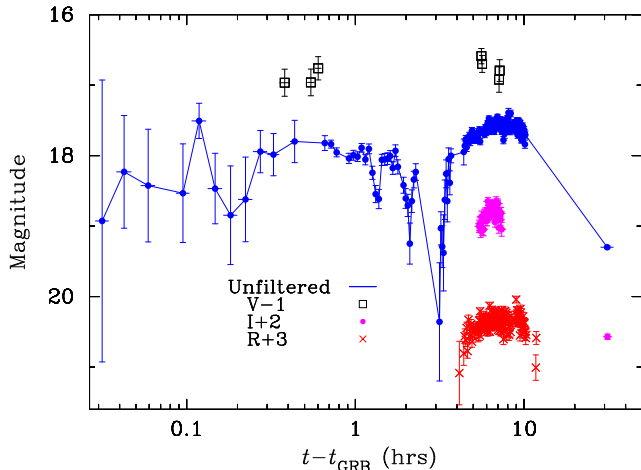


Figure 2. MASTER optical light curves of GRB 100901A in different filters: *R* (3 mag added; red crosses), *I* (2 mag added; magenta dots), *V* (1 mag subtracted; black squares), and unfiltered (blue dots connected with solid line). Magnitudes are not corrected for the Galactic extinction. Horizontal bars show exposures.

Table 2. MASTER upper limits on the optical flux obtained with the polarizing filter for GRB 100902A. The bottom row is coadded from all above.

t_{start} (UT)	t_{end} (UT)	Exposure time (s)	$t_{\text{start}} - T_0$ (s)	mag
19:33:38	19:33:58	20	104.0	17.0
19:34:12	19:34:42	30	132.0	17.3
19:34:57	19:35:57	40	177.0	17.3
19:35:51	19:36:41	50	231.0	17.4
19:33:38	19:36:41	140	104.0	18.0

about 200 s after the trigger time, and MASTER was first to witness its active stage in the optical waveband. The imaging was attempted at two polarization angles with 20 s exposure times. However, no optical transient was found at the XRT position with the upper limit of 17 mag (Krushinski et al. 2010a). The final results of our photometry (Gorbovskoy et al. 2010), which are the upper limits on the optical flux at two polarization angles, are summarized in Table 2. The GRB position was observed by the OSN at ~ 7 h after the trigger with an upper limit on the magnitude in *I*-band: ~ 21.8 mag (Tello et al. 2010).

2.3 Early optical observations of GRB 100905A

On September the 5th, a GRB was detected by *Swift*/BAT at 15:08:15 UT (Marshall et al. 2010). The Tunka MASTER telescope was pointed to its position 55 s after T_0 . The imaging was carried out at two polarization angles (Ivanov et al. 2010c). No optical transient is found. Upper limits are given in Table 3. The further optical observations were carried out by UVOT (Siegel & Marshall 2010) and the 1.5-m telescope of the Observatorio de Sierra Nevada (Sota, de Ugarte Postigo & Castro-Tirado 2010) and yielded no optical counterpart either. Barthelmy et al. (2010a) obtained that $T_{90} = 3.4 \pm 0.5$ s implying that our

Table 3. MASTER upper limits on the optical flux obtained with polarizing filter for GRB 100905A.

t_{start} (UT)	t_{end} (UT)	Exposure time (s)	$t_{\text{start}} - T_0$ (s)	mag
15:09:10	15:09:20	10	55.0	16.5
15:09:39	19:09:59	20	84.0	17.1
15:10:45	15:11:15	30	150.0	17.3
15:11:35	15:12:15	40	200.0	17.5

observations can be qualified as ‘early’, not prompt. This γ -ray burst might belong to the class of intermediate duration GRBs, separated from the class of long GRBs on statistical grounds by Horváth (1998, 2002); Mukherjee et al. (1998). While underlying physical properties of the subclasses of long GRBs appear to be similar (type of progenitor, interstellar environment), there is an evidence for duration and luminosity differences caused by some slight diversity of the bursts (de Ugarte Postigo et al. 2011).

2.4 Prompt and afterglow optical observations of GRB 100906A

At 13:49:27 UT, September the 6th, GRB 100906A was detected (Markwardt et al. 2010). The BAT/*Swift* detected several bright peaks with $T_{90} = 114.4 \pm 1.6$ s (Barthelmy et al. 2010b). GRB 100906A has been also observed by the *Konus-Wind* starting from 13:49:30 UT (Golenetskii et al. 2010).

Two MASTER telescopes, at Tunka and Blagoveschensk, were pointed to the GRB position, respectively, 38 s after the BAT trigger time T_0 and 58 s after T_0 . As a pilot instrument was mounted at the time at the Blagoveschensk site⁶, we present only the data obtained by the telescope at Tunka. In Kourovka and Kislovodsk, the weather conditions were not suitable for observations.

A bright optical transient was localized by MASTER at the *Swift*/UVOT position (Markwardt et al. 2010), 13 mag at maximum. During the first hour after the trigger time, 24 images in unfiltered light at two polarization angles were produced by the Tunka telescope. Fig. 3 shows the early observations of GRB 100906A in optical, 0.3–10 keV, and 15–150 keV energy range (also Fig. 4 and Table 4). A movie of the optical burst of GRB 100906A as seen at Tunka is available on the web⁷.

We calculate the relative difference between the signals coming from the two polarization filters, for the time interval $100 - 10^4$ s after T_0 . It is less than the relative measuring accuracy of filters 2 per cent, estimated through the observations of standard stars. Unfortunately, technical limitations do not allow us to draw a decisive conclusion about the polarization degree of GRB 100906A (see § 5.1 and the Appendix).

The 1.5m OSN telescope at Sierra Nevada observed the GRB few hours after T_0 (Fig. 5 and Table 5). Calibration

⁶ Since December 2010, the Blagoveschensk telescope is in a full operating mode.

⁷ <http://master.sai.msu.ru/static/GRB/grb100906.avi>

Table 4. Photometry data for GRB 100906A by MASTER in the unfiltered band with two orthogonal polarizing filters. Full table can be found online in the electronic issue.

P_{\downarrow}			P_{\leftrightarrow}		
$t - T_0$ (h)	Exp. (s)	Unfiltered (mag)	$t - T_0$ (h)	Exp. (s)	Unfiltered (mag)
0.013495	10	15.30 ± 0.04
0.021896	10	13.62 ± 0.03	0.023187	10	13.53 ± 0.03
0.032043	20	13.42 ± 0.03	0.033377	20	13.44 ± 0.03
0.044763	30	13.53 ± 0.03	0.046099	30	13.55 ± 0.03
0.060409	40	13.69 ± 0.03	0.061662	40	13.75 ± 0.03
0.078794	50	13.88 ± 0.03	0.080028	50	13.94 ± 0.03
0.099815	60	14.19 ± 0.03	0.101093	60	14.25 ± 0.03
0.123506	70	14.42 ± 0.03	0.124784	70	14.46 ± 0.03
0.152931	90	14.68 ± 0.03	0.154302	90	14.71 ± 0.03
0.189999	110	14.96 ± 0.03	0.191257	110	14.95 ± 0.03

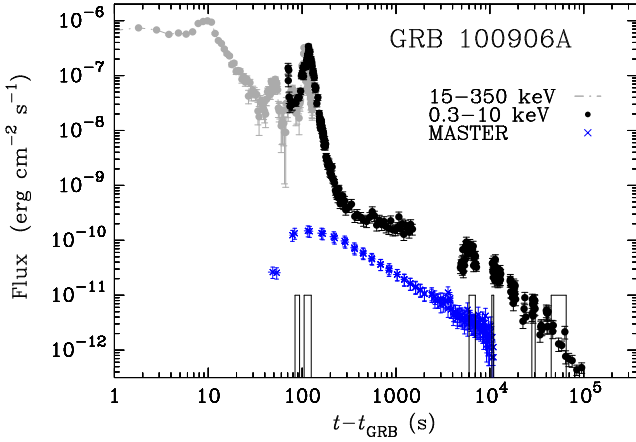


Figure 3. GRB 100906A optical light curve obtained by MASTER with one polarization filter (blue dots with 20 per cent error bars resulted due to uncertainty of magnitude-flux conversion, see § 3.2; data are corrected for the Galactic extinction) along with the *Swift*/BAT 15-350 keV flux with 1 s binning (grey dots connected with dot-dashed line; data with negative lower limits are not shown) and the *Swift*/XRT 0.3-10 keV unabsorbed-flux light curve (black dots; Beardmore & Markwardt 2010). Thin-line rectangles show the time intervals selected for spectral analysis.

for *BVIR* bands is done using 49 USNO stars, and for *U*-band using a Landolt star observation. Aperture photometry is carried out using *phot* as implemented in IRAF with a radius equal to the seeing. The error of the afterglow magnitude was obtained adding quadratically the statistical error given by *phot* and the zero point error determined with the 49 field reference stars. In addition, Table 6 shows the late photometry obtained by the 2.56-m Nordic Optical Telescope (NOT).

The redshift of the host galaxy $z = 1.727$ was obtained with the Gemini-North telescope (Tanvir, Wiersema & Levan 2010).

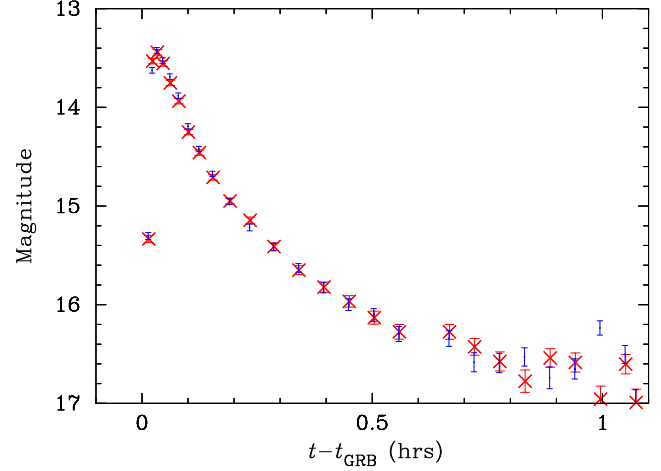


Figure 4. MASTER light curve of GRB 100901A in two polarizations, unfiltered band (blue dots and red crosses). Data are not corrected for the Galactic extinction.

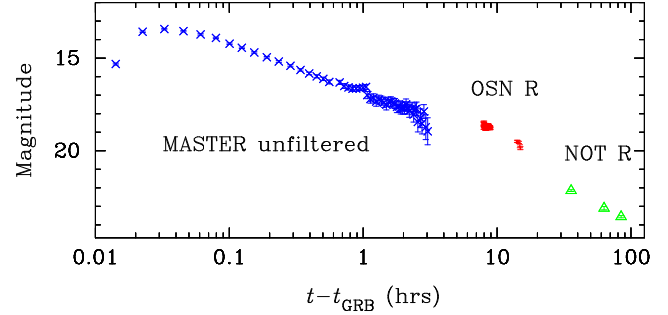


Figure 5. OSN and NOT telescopes *R*-band light curve of GRB 100906A (red bars and green triangles with small error bars, respectively). MASTER unfiltered band, one polarization light curve is plotted by blue crosses before 5 h. All data are not corrected for the Galactic extinction.

Table 5. *UBVRI*-photometry for GRB 100906A obtained by the OSN telescope. Reported times are middle times of exposures. Dots substitute 50 observations that can be found online in the electronic version.

Band	$t - T_0$ (h)	Exposure time (s)	Magnitude
R	7.920835	36	18.53 ± 0.12
R	7.935742	36	18.72 ± 0.12
...
R	8.895094	60	18.79 ± 0.06
R	14.091390	180	19.49 ± 0.06
R	14.217964	180	19.50 ± 0.06
R	14.540464	180	19.55 ± 0.06
R	14.784353	180	19.76 ± 0.08
R	14.928057	180	19.86 ± 0.08
R	38.528342	2×300	> 21.5
V	14.141108	180	19.91 ± 0.20
V	38.402228	300	> 21.0
B	14.193888	300	20.65 ± 0.22
B	38.318343	5×300	> 21.0
I	14.278609	2×180	19.46 ± 0.12
U	14.571669	2×900	> 17.5
U	38.234160	300	> 16.5

Table 6. R-magnitudes of GRB 100906A obtained by NOT.

$t_{\text{start}} - T_0$ (h)	$t_{\text{end}} - T_0$ (h)	Exp. time (s)	R (mag)
35.031028	36.338862	3×600	22.15 ± 0.05
62.828250	63.078251	900	23.10 ± 0.09
84.046943	84.763888	2×900	23.56 ± 0.06

Table 7. Upper limits on the optical flux in V-band for GRB 101020A obtained for coadded images.

$t_{\text{start}} - T_0$ (s)	t_{middle} (s)	Exp. time (s)	V (mag)	Coadded number
106	116	20+20	14.9	1+1
472	2836	4300	18.5	25

2.5 Limits on the prompt and afterglow optical flux of GRB 101020A

On October the 10th, at 23:40:41 UT, the *Swift*/BAT triggered and located GRB 101020A (Saxton et al. 2010). Sakamoto et al. (2010a) found $T_{90} = 175 \pm 28$ s. MASTER telescope at Kourouka was pointed to the GRB 101020A position 106 s after T_0 at a large zenith distance of 80 degrees (Krushinski et al. 2010b,c). It was observed with two optical tubes. No optical transient is detected with the upper limits in V-band reported in Table 7, where magnitudes are obtained from coadded images.

3 DATA REDUCTION AND ANALYSIS FOR GRB 100901A AND GRB 100906A

3.1 MASTER astrometric and photometric calibration

Each MASTER telescope is equipped with a set of Johnson/Bessell filters and two linear polarizing laminated films. For every image, astrometric calibration using `imcoords` of IRAF v2.14 is performed. Aperture photometry is done with the `phot` of IRAF package (Tody 1993). Standard stars from 13.5^m to 17^m are selected from the Sloan Digital Sky Survey Data Release 7 (SDSS-DR 7) (Abazajian et al. 2009). Influence of atmospheric transparency variations on instrumental stellar magnitudes is eliminated following an algorithm described in Everett & Howell (2001). Stars with variations exceeding threefold the errors calculated by IRAF from signal-to-noise information are expelled from the list, and the remaining standard stars are related to SDSS-DR7 data as suggested by Lupton (2005)⁸:

$$\begin{aligned}
 B &= g + 0.1884(u - g) + 0.1313, \\
 V &= g - 0.5784(g - r) - 0.0038, \\
 R &= r - 0.2936(r - i) - 0.1439, \\
 I &= i - 0.3780(i - z) - 0.3974,
 \end{aligned} \tag{1}$$

where *BVRI* are the Johnson system and *i*, *r*, *g*, and *z* are the Sloan Survey photometric system (all in the Vega

system). Resulting lists of standard stars are given in Table 8 for GRB 100901A and in Table 9 for GRB 100906A. Associated variances⁶ between observed and catalogue values after applying the above relations in different filters are 0.005 – 0.008^m. In our observations, standard deviations of light curves of the standard stars are greater, 0.02 – 0.1 mag depending on the filter. For images obtained in the unfiltered band, we use a zero-point correction to the unfiltered magnitudes obtained at the Kislovodsk MASTER telescope. Flux calibration of the unfiltered magnitudes at Kislovodsk is described in Section 3.2.

The GRB magnitude errors are defined by the standard deviation of the brightness variations of the standard stars of similar magnitude in the case of high signal-to-noise ratio. At the low signal-to-noise ratio, we lack standard stars of such magnitudes. To estimate observational errors, we take the theoretical limit for errors following the basic CCD equation. This limit is much greater (up to 2 mag at mag > 18) than expected amplitude variations of standard stars at such signal-to-noise level.

For each of the standard stars, we evaluate the difference between its average magnitudes in both orthogonal polarizations. Assuming that the light of standard stars should not be polarized, the standard stars with outlier polarization are expelled from the list. Afterwards, corrections are applied to match average magnitudes of the standard stars in two polarizations. The relative accuracy of observations with two filters is approximately 2 per cent, basing on observations of standard stars.

3.2 MASTER flux calibration

To convert magnitudes *BVRI* into absolute values, we use the zero-magnitude flux densities of the Landolt photometry (see, e.g., Pickles & Depagne 2010). To convert CCD photometry into absolute fluxes without color filter interposed, that is, in a wide waveband (see Fig. 6), we use the Pogson formula relating stellar magnitudes and CCD band-integrated flux with a zero-magnitude flux calculated using the Vega spectrum as given by Hayes (1985).

The standard stars are designated with the *W* and *P* magnitudes: obtained from observations in the wide waveband and in the wide waveband plus polarizer. Both are approximated by the formula $0.8R + 0.2B$. This formula is arrived at by compilation of color diagrams $W - X$ versus $B - R$, where X is a combination of stellar magnitudes, $X = aR + bB$. In a general case, points group around a straight oblique line. The zero-slope of the relation is achieved by fitting for the parameters *a* and *b*. It is found that for the white light the above representation of the wide-band magnitudes holds with an accuracy of 4 per cent for *W*-magnitudes and 2 per cent, for *P*-magnitudes. Unfortunately, for a polarizer that we used in the observations there was a long-wavelength interval with unspecified transmission efficiency function. Simulating polarizer transmission function in different ways and folding it with different spectra (Vega's, $\propto \nu^{-1}$, and $\propto \nu^0$), we have estimated the maximum additional uncertainty of ~ 20 per cent. Thus we add 20 per cent of uncertainty when we convert *P* to absolute fluxes.

Observed magnitude *W* of an investigated source is converted into the absolute flux values using the Pogson equation

⁸ <http://www.sdss.org/dr7/algorithms/sdssUBVRITransform.html>

$$F_{\text{GRB}}^W = F_o^W \times 10^{-0.4W}, \quad (2)$$

where F_o^W is the calculated Vega flux in the CCD spectral band:

$$F_o^W = \int F_{\text{Vega}}(\lambda) W(\lambda) d\lambda = 1.33 \times 10^{-5} \text{ erg cm}^{-2} \text{ s}^{-1}. \quad (3)$$

In the same way, magnitudes P are converted to flux values using eq. (2) with the zero-magnitude flux

$$F_o^P = \int F_{\text{Vega}}(\lambda) P(\lambda) d\lambda = 1.16 \times 10^{-5} \text{ erg cm}^{-2} \text{ s}^{-1}. \quad (4)$$

In the above expressions, $W(\lambda)$ and $P(\lambda)$ are, respectively, the normalized CCD-response function and its normalized convolution with the transmission efficiency of the polarizer (see the right panel of Fig. 6). Of course, if one observes a source with partly (linearly) polarized light through such polarization filter, one needs a full information on the degree of polarization and its angle to derive the total flux. For an unpolarized source, or for a source with equal signals from two polarizers (the case of GRB 100906A), we can safely use formula (4). For details we refer to Appendix.

To obtain GRB's flux density at the wavelength of the CCD-response maximum, 5500 Å, we divide flux F_{GRB}^W or F_{GRB}^P by an effective frequency interval $\Delta\nu_{\text{eff}}$ of the corresponding response function. Naturally, the value of $\Delta\nu_{\text{eff}}$ depends on a particular spectral distribution. The effective frequency interval of the CCD-response function is $\sim 3.9 \times 10^{14}$ Hz, calculated as the mean of values $\Delta\nu_{\text{eff}}$ for the Vega spectrum, white light, and power-law spectrum with -1 slope, all falling inside a 15 per cent uncertainty interval. The effective frequency interval of the CCD plus polarizer, calculated in the same way, is $\sim 3.2 \times 10^{14}$ Hz with a 10 per cent uncertainty interval. Bearing in mind that a real spectrum might be something different from the three considered in such simple analysis, we assume approximately a 20 per cent accuracy for converting from flux units to spectral flux density units.

3.3 *Swift* BAT and XRT light curves

In order to build flux light curves observed by *Swift*/BAT (Figs. 1 and 3), standard sets of GRB products are obtained using the tool **batgrbproduct** within HEASOFT v6.10, and the count light curves in 15–350 keV are retrieved. The 15–150 keV spectra averaged over the total-fluence time interval are analysed in XSPEC (Arnaud 1996) using the power-law approximation. The derived spectral parameters are used to calculate 15–350 keV model flux and to obtain counts to flux conversion factors in the 15–350 keV range. Thus we apply constant conversion factors 1.07×10^{-6} erg cm $^{-2}$ counts $^{-1}$ for GRB 100901A and 9.17×10^{-7} erg cm $^{-2}$ counts $^{-1}$ for GRB 100906A.

The *Swift*/XRT 0.3–10 keV unabsorbed light curves are available from the *Swift* Burst Analyser. These light curves are produced with information on spectral evolution involved (Evans et al. 2010). The late-time spectra of GRBs, available from the *Swift* Spectra Repository, are the source of estimates of the column densities for the soft X-ray absorption.

3.4 Spectral fitting

In order to build simultaneous wide-energy spectra, we select time intervals, which are covered by the optical observations. The prompt stage of GRB 100901A (before T_{90}) contains three suitable MASTER exposure intervals: $t - T_0 = 193 - 233$, $312 - 372$, and $387 - 467$ s, where T_0 is the trigger time. There are two MASTER time intervals during the prompt stage of GRB 100906A overlapping with the observations by *Swift*/XRT, 73.8–83.8 s and 105–125 s (or very close, in the first case).

We download the X-ray time-sliced spectra, constructed for the time intervals of the optical exposures, from the *Swift* spectra repository (Evans et al. 2009). For GRB 100906A we also use the results obtained by the *Konus-Wind* (Golenetskii et al. 2010). BAT spectra and response matrices are prepared as described in the Data Analysis Guidelines⁹. They are extracted for the selected time intervals and corrected using the tasks **batbinevt**, **batupdatephakw**, **batphasyserr**, and a response matrix generated by the **batdrmggen** task. Then the spectra are fitted in XSPEC v12.6 using models **powerlaw** (power law), **cutoffpl** (cut-off power law), or **grbm** (Band function), in combination with absorption components. When simultaneous fits for the 0.3–10 keV and 15–150 keV and/or optical data are performed, XRT spectra are rebinned using **grppha** to ensure that there are at least 20 counts per bin, which is needed for joint minimization of χ^2 .

To account for the soft X-ray absorption, we use XSPEC model component **phabs** (Galactic absorption) and **zphabs** (absorption in the host galaxy). When we fit the parameters of the optical extinction in the GRB host, we use the XSPEC model **zdust**, which is the extinction by the dust grains. In the fits, whose results are presented in the tables in the next section, we assume the Small Magellanic Cloud (SMC) type of the host galaxy extinction curve and the total-to-selective extinction $R_V = 2.93$ (Pei 1992) following results of the studies by Jensen et al. (2001); Schady et al. (2010). We discuss variations due to the different extinction laws in the text. Correction for the reddening in the Galaxy is done beforehand, using the values calculated using the NED Galactic Extinction calculator¹⁰ based on a work of Schlegel, Finkbeiner & Davis (1998).

To analyse the late-time spectra, we consider the optical observations after $10 T_{90}$. First, we check that big variations of X-ray flux are absent in a time interval: we request that the flux density at 10 keV varies less by a factor of 3. The X-ray data is rebinned to a minimum of 10 (20, if possible) counts per bin (by **grppha**). The optical data is averaged over the time interval and transformed by the task **flx2xsp**. We check that the number of degrees of freedom in the fit by the XSPEC model **phabs*zphabs*zdust*powerlaw** is more than 5. Thus selected time intervals are depicted by rectangles in Figs. 1, 3, and 11.

⁹ <http://swift.gsfc.nasa.gov/docs/swift/analysis/threads/batgrbproductthread.htm>

¹⁰ <http://ned.ipac.caltech.edu/forms/calculator.html>

Table 8. Stars from SDSS-DR7 catalogue used as standard stars for GRB 100901A. Columns 3–7 contain SDSS *ugriz* magnitudes (Vega system). Column 8 contains average unfiltered *W*-band MASTER magnitude. Full table can be found online in the electronic issue.

Source ID	SDSS name	<i>u</i> (mag)	<i>g</i> (mag)	<i>r</i> (mag)	<i>i</i> (mag)	<i>z</i> (mag)	<i>W</i> (mag)	RA J2000 (d)	DEC J2000 (d)
1	J014906.68+224024.7	19.246	17.05	15.96	15.462	15.161	15.95	27.277834	22.673535
2	J014904.39+224045.3	15.841	14.609	14.143	13.953	13.897	14.21	27.26829	22.679256

Table 9. Standard stars used for the photometry of GRB 100906A. Column 3 contains average unfiltered *P*-band MASTER magnitude measured with one of polarization filters. Full table can be found online in the electronic issue.

Source ID	USNO-A2.0 name	P_{\uparrow} (mag)	Standard deviation of light curve (mag)	$\langle P_{\uparrow} \rangle - \langle P_{\leftrightarrow} \rangle$ (mag)	RA J2000 (d)	DEC J2000 (d)
(1)	(GRB 100906A)	...	1.14	0.01	28.68413	55.63050
2	1425-02624804	15.70	0.04	-0.04	28.69122	55.63834

4 RESULTS

4.1 Spectra of GRB 100901A and GRB 100906A before T_{90}

For the three early spectra of GRB 100901A (Fig. 7), fits with absorbed power-law are satisfactory (Fits 100901.1, 100901.2, and 100901.3 in Table 10). Other spectral models, cut-off power law and the Band function, do not improve the fitting statistics.

For GRB 100906A, we do not include the host-galaxy absorption model component, as its spectral distributions from the optical to X-rays (Fig. 8) cannot apparently be fitted by a single power law. Generally, for a variable complex spectrum of an early GRB emission, it is impossible to estimate the extinction in the optical band, as one can use no a-priori information about the spectral distribution. Table 11 contains the parameters of the fits by the Band model, together with the resulting values of χ^2 for the alternative models with fewer free parameters, which give worse results. We also calculate the slopes of the photon spectrum between the MASTER points and the best-fit 3 keV flux densities (column 3 in Table 11). We remind that the optical points are corrected for the Galactic extinction.

Apparently, the peak of the spectral energy distribution (SED) of GRB 100906A is located somewhere around 0.3–30 keV at times 80–120 s and moves gradually to the soft energies. The SED-peak energy E_{peak} for the Band spectrum is $(-\alpha_B + 2) \times E_0$, where α_B is the photon index of the lower-energy part of the Band function, and E_0 is the characteristic energy for the Band function (Table 11). We obtain that E_{peak} shifts from about 30 to 4 keV between the two spectral distributions presented in Fig. 8. The higher energy part of the spectrum of GRB 100906A (> 30 keV) can be fitted by a single power law. This is consistent with the Konus–Wind results (Fig. 8, dotted line). According to Golenetskii et al. (2010), the spectrum of the second bursting episode of GRB 100906A observed by Konus–Wind in γ -rays from 98.304 to 122.880 s is best fitted in the 20 keV–2 MeV range by a power-law model with the photon index $2.55^{+0.25}_{-0.2}$.

4.2 Host galaxy extinction of GRB 100901A

We fit several late-time spectra comprised of the XRT/*Swift* data and simultaneous optical points available from MASTER. The optical points are the time-averaged unfiltered *W* magnitudes as follows: 18.05 ± 0.03 , 17.78 ± 0.02 , 17.61 ± 0.04 , and 19.30 ± 0.02 mag, corrected for the Galactic extinction $A_V = 0.327$ (NED; Schlegel, Finkbeiner & Davis 1998), successively for the fits in Table 12. As well as for the prompt spectra, we can approximate the late-time spectra of GRB 100901A by an absorbed power-law model.

Averaging results of the late-time fits (Table 12), we obtain $A_V^{\text{int}} = 0.4 \pm 0.2$ and $N_H^{\text{int}} = (2.2 \pm 0.7) \times 10^{21} \text{ cm}^{-2}$. Averaging results of the three early fits (Table 10), we obtain $A_V^{\text{int}} = 0.8 \pm 0.1$ and $N_H^{\text{int}} = (5.1 \pm 0.6) \times 10^{21} \text{ cm}^{-2}$. There is an apparent change in values of N_H^{int} and A_V^{int} between the prompt-time and late-time fit parameters. It is likely that the prompt-time value of N_H^{int} is biased because of the spectral evolution and, probably, because the prompt spectral shape is not precisely power-law in the range from the optical to X-rays. Butler & Kocevski (2007) and Evans et al. (2010) argue that absorption derived from early-time XRT data, when a strong spectral evolution is present, can be misleading.

The late-time spectrum compiled at the XRT/*Swift* spectrum repository (UK *Swift* Science Data Centre) for 4000–33229 s yields the value of the intrinsic $N_H^{\text{int}} = (2.9 \pm 0.9) \times 10^{21} \text{ cm}^{-2}$ (90 per cent uncertainty interval), which is in a very good agreement with our fit results for the late-time sliced spectra. This indicates that a power law approximation for the X-ray spectrum of GRB 100901a is indeed a good approximation for any late time interval.

We have also tried other types of extinction laws in the GRB host. In addition to the fits, presented in Table 12, we performed fits with different extinction laws in the host galaxy: that of the LMC (Large Magellanic Cloud) and MW (Milky Way). For them we applied different values of R_V (Pei 1992, see below). The quality of the fits remains the same and the values of N_H as well, because the choice of the optical extinction does not affect strongly the amount of the soft X-rays absorption. We have found that depending on the extinction law applied, for three late-time intervals,

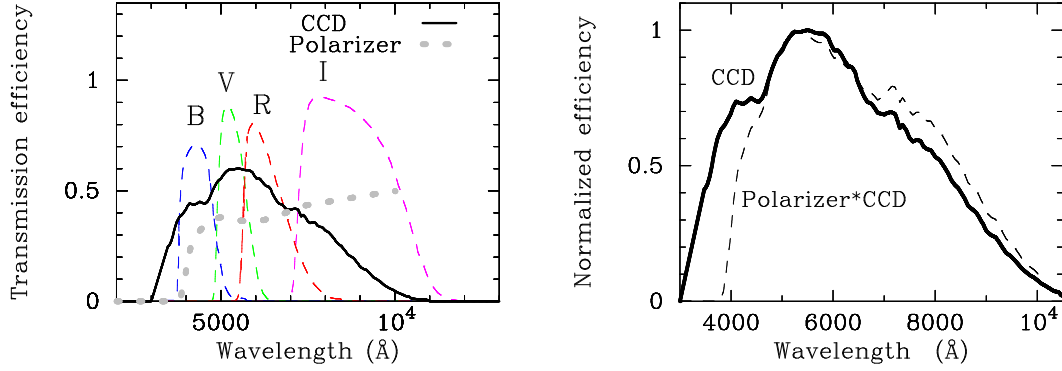


Figure 6. In the left panel the MASTER filter transmission efficiencies are plotted along with those of the CCD and polarizer. In the right panel, functions $W(\lambda)$ and $P(\lambda)$ are shown, which are the bandpasses of the CCD and of the CCD plus polarizer, respectively.

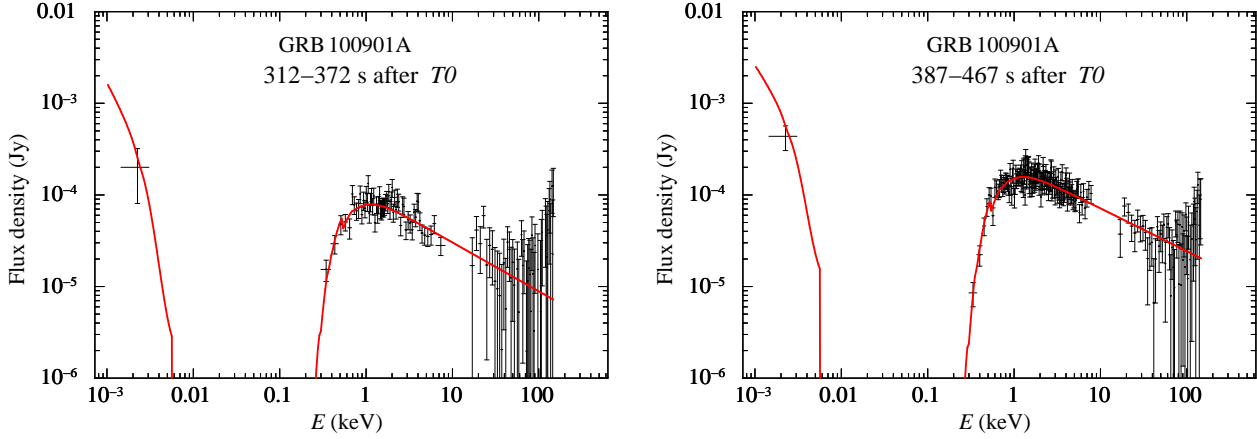


Figure 7. Spectrum of GRB 100901A for two time intervals at $t \gtrsim T_{90}$. Optical flux density obtained by MASTER, corrected for the Galactic extinction $A_V = 0.327$ (NED; Schlegel, Finkbeiner & Davis 1998), is shown by the single left point, whose horizontal bar corresponds to the MASTER unfiltered effective frequency interval. Spectra in 0.3–10 and 15–150 keV are made with the *Swift* BAT and XRT data. Best-fitting absorbed power laws are shown by the red lines. Their spectral parameters are described in Table 10 as Fit 100901.2 for 312 – 372 s and Fit 100901.3, for 387 – 467 s).

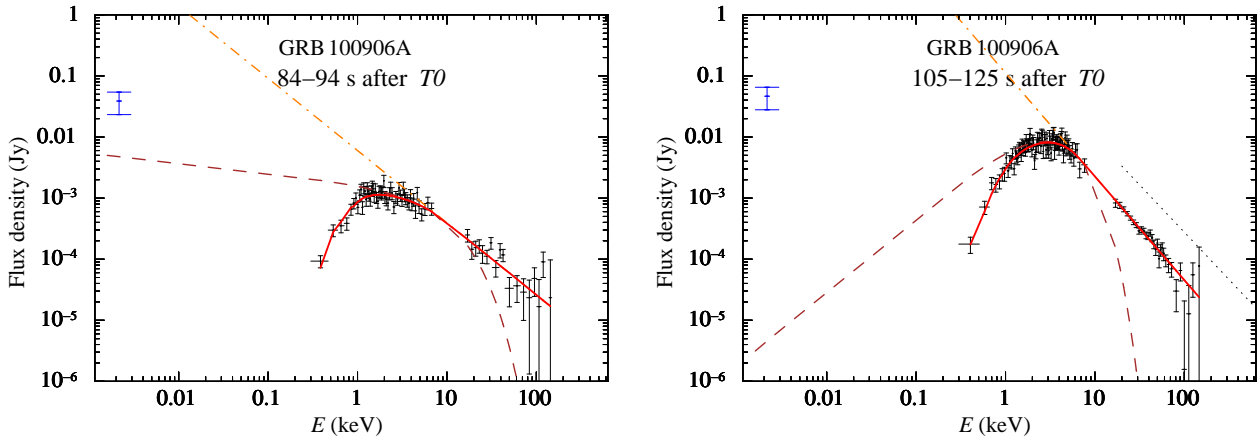


Figure 8. Spectrum of GRB 100906A for two time intervals at $t \gtrsim T_{90}$. Optical points are corrected for the Galactic extinction $A_V = 1.194$ (NED; Schlegel, Finkbeiner & Davis 1998). In the left panel, we use the MASTER observation at 73.8–83.8 s. Best-fitting absorbed Band functions are shown by the red lines (Fit 100906.1 and 100906.2 in Table 10). No attempt has been made to estimate the optical extinction in the GRB host galaxy. The brown dashed line depicts the unabsorbed low-energy part, and the orange dot-dashed line, the unabsorbed high-energy part. Dotted power law represents observations of Konus-*Wind* from 98.304 to 122.880 s in 20 keV–2 MeV with a correct slope and a roughly estimated flux.

Table 10. Spectral parameters for GRB 100901A at the prompt stage resulted from the simultaneous fitting of the absorbed power law in XSPEC (`phabs*zphabs*zdust*powerlaw`) to the MASTER, XRT, and BAT data (Fig. 7). Galactic absorption column density is fixed at $N_{\text{H}} = 7.1 \times 10^{20} \text{ cm}^{-2}$ (Kalberla et al. 2005). Assumed host galaxy extinction curve is SMC type and the total-to-selective extinction is $R_V = 2.93$. The 4th and 5th columns give the fitted intrinsic absorption column density and optical extinction at $z = 1.408$, respectively.

Fit ID	$t - T_0$ (s)	Photon index	$N_{\text{H}}^{\text{int}}$ (10^{22} cm^{-2})	A_V^{int}	χ^2/dof
100901.1	193 – 233	1.60 ± 0.08	0.6 ± 0.2	$1.1^{+0.6}_{-0.3}$	73.4/94
100901.2	312 – 372	1.53 ± 0.05	0.4 ± 0.1	$0.95^{+0.4}_{-0.2}$	138/134
100901.3	387 – 467	1.49 ± 0.02	0.55 ± 0.07	0.75 ± 0.1	216/219

Table 11. Spectral parameters for GRB 100906A at the prompt stage resulted from the fitting of the absorbed Band function in XSPEC (`phabs*zphabs*grbm`) to the XRT and BAT data (Fig. 8). Galactic absorption column density is fixed at $N_{\text{H}} = 2.2 \times 10^{21} \text{ cm}^{-2}$ (Kalberla et al. 2005). Column 3 gives the photon index between the optical and modeled 3 keV flux density; next columns: the photon indices and characteristic energy of the Band function, intrinsic absorption at $z = 1.727$. In the last three columns statistics χ^2 of the fits shown in Fig. 8 are typed in **bold**, statistics of fits with the alternative models are typed in normal font.

Fit ID	$t - T_0$ (s)	MASTER-XRT 2.2 eV–3 keV	Photon indices of Band function		E_0 (keV)	$N_{\text{H}}^{\text{int}}$ (10^{22} cm^{-2})	χ^2/dof Band	χ^2/dof power law	χ^2/dof cut-off pow
100906.1	84 – 94 [†]	1.50 ± 0.06	1.2 ± 0.2	$2.18^{+0.08}_{-0.07}$	9^{+7}_{-4}	$0.1^{+0.3}_{-0.1}$	112/110	141/112	121/111
100906.2	105 – 125	1.24 ± 0.06	$-0.22^{+0.24}_{-0.07}$	2.70 ± 0.03	$2.3^{+0.4}_{-0.1}$	$0^{+0.23}_{-0.0}$	149/139	314/141	254/140

[†] MASTER observation was carried out in an slightly earlier time interval, 73.8–83.8 s.

the average total extinction $A_V^{\text{int}} = R_V E(B - V)^{\text{int}}$ varies as: $\langle A_V^{\text{int}} \rangle = 0.4 \pm 0.2$ (SMC, $R_V = 2.93$), $\langle A_V^{\text{int}} \rangle = 0.5 \pm 0.2$ (LMC, $R_V = 3.16$), and $\langle A_V^{\text{int}} \rangle = 0.7 \pm 0.2$ (MW, $R_V = 3.08$).

Basing on the ‘late-time’ values of the optical extinction in the GRB host we calculate the ratio $N_{\text{H}}^{\text{int}}/A_V^{\text{int}}$. It equals $(5 \pm 2) \times 10^{21} \text{ cm}^{-2}$ (for the SMC type of the extinction in the GRB host), $(4 \pm 2) \times 10^{21} \text{ cm}^{-2}$ (LMC) and $(3 \pm 1) \times 10^{21} \text{ cm}^{-2}$ (MW). These are not far from the ratios empirically found for the Milky Way and Magellanic Clouds: $\sim 4 \times 10^{21}$ (SMC), $\sim 3.5 \times 10^{21}$ (LMC), and $\sim 2 \times 10^{21} \text{ cm}^{-2}$ (MW) (e.g., Schady et al. 2010). Thus, independently of the extinction law used, the resulting metal-to-dust ratio in the host of GRB 100901A is comparable to the level measured for the Milky Way or Magellanic Clouds.

4.3 Host galaxy extinction of GRB 100906A

Three late-time spectral distributions are shown in Figs. 9 and 10. The parameters of the fits are listed in Table 13. The optical points are the time-averaged unfiltered P magnitudes by MASTER: 17.54 ± 0.05 for 6000 – 7000 s, 18.7 ± 0.3 for 10500–11000 s; OSN $R = 18.70 \pm 0.02$ for 28000–30400 s. The optical point in the R -band at 50000–54000 s is obtained by averaging the OSN data ($R = 19.7 \pm 0.3$) and V, B, I points can be found in Table 5. Before the fitting, the optical data are corrected for the Galactic extinction calculated in the NED Extragalactic Calculator: $A_V = 1.194$, $A_B = 1.554$, $A_R = 0.963$, and $A_I = 0.699$ (NED; Schlegel, Finkbeiner & Davis 1998).

One can see that the optical data at ~ 14 h (Fig. 10) is best fitted by an absorbed broken power-law with a peak in the optical range. However, we cannot consider this peak robust because the optical points are non-simultaneous and there is a strong variation observed in the R -band around 14 h (see Fig. 5).

The parameters of the Fit 100906.3 (the first three lines in Table 13) are obtained by simultaneously fitting the data

for the three time intervals with the spectral slope and normalization left independent and tied $E(B - V)^{\text{int}}$ (that is, A_V) and $N_{\text{H}}^{\text{int}}$. This was done in an attempt to increase statistics to obtain positive 1σ interval for A_V^{int} . Nevertheless, we can report only the 2σ upper limit. Setting other types of the extinction law in the host galaxy does not change its value.

The spectrum of GRB 100906A at 10–50 ks interval from the XRT spectrum repository (at the UK *Swift* Science Data Centre) yields the value of intrinsic $N_{\text{H}}^{\text{int}} = (8.5 \pm 3) \times 10^{21} \text{ cm}^{-2}$ (with 90 per cent uncertainty interval). The values of $N_{\text{H}}^{\text{int}}$ in Table 13 with 1σ errors are consistent with this value. If we take the lower 2σ limit of the XRT repository value, $N_{\text{H}}^{\text{int}} = 4.8 \times 10^{21} \text{ cm}^{-2}$, and the upper 2σ limit on A_V^{int} obtained for different extinction laws, we arrive at the lower 2σ limit on $N_{\text{H}}^{\text{int}}/A_V^{\text{int}} \approx 1.1 \times 10^{22}$. This limit is at least twice the typical ratios, empirically defined for the Milky Way and Magellanic Clouds (see § 4.3). This ratio is consistent with the results of Schady et al. (2010) who studied 28 GRBs and found values of $N_{\text{H}}^{\text{int}}/A_V^{\text{int}}$ typically higher than those for the Milky Way and Magellanic Clouds.

We conclude that for GRB 100906A our fitting provides only the upper limit on A_V^{int} , and that there are indications that this GRB has high $N_{\text{H}}^{\text{int}}/A_V^{\text{int}}$ ratio, which can be due to a dust destruction or the intrinsic properties of the host galaxy.

4.4 Jet break time of GRB 100906A

We construct broken power-law fits to the light curves of GRB 100906A after 10 ks. Table 14 presents the parameters of the fits. A break on the X-ray light curve is found around ~ 50 ks. The parameters of the 0.3 – 10 keV light curve can be reconciled with the ‘closure relations’ between the temporal and spectral indices (α and β in $F_\nu \propto t^{-\alpha} \nu^{-\beta}$) in the framework of the fireball model in the following way

Table 12. Spectral parameters for GRB 100901A at late time intervals. XSPEC fitting of the absorbed power law to the MASTER and XRT/*Swift* data is performed. Frozen fit parameters are the same as for the fits in Table 10.

Fit ID	$t - T_0$ (s)	Photon index	$N_{\text{H}}^{\text{int}}$ (10^{22} cm^{-2})	$A_{\text{V}}^{\text{int}}$	χ^2/dof
100901.4	5000 – 6500	2.1 ± 0.1	0.3 ± 0.1	$0.8^{+0.5}_{-0.4}$	15.8/14
100901.5	15000 – 17500	2.0 ± 0.1	$0.1^{+0.2}_{-0.1}$	$0.2^{+0.3}_{-0.2}$	38.6/38
100901.6	27000 – 28500	2.1 ± 0.1	0.3 ± 0.2	$0.4^{+0.4}_{-0.3}$	36.6/35
100901.7	102800 – 121500	$2.10^{+0.01}_{-0.11}$	0.28 ± 0.25	$0.5^{+0.8}_{-0.2}$	13.0/10

Table 13. Spectral parameters for GRB 100906A at several late time intervals (Figs. 9 and 10). XSPEC fitting of the absorbed power law or broken power law to the MASTER, OSN, and XRT/*Swift* data is performed. Galactic absorption column density is $N_{\text{H}} = 2.21 \times 10^{21} \text{ cm}^{-2}$ (Kalberla et al. 2005). The host galaxy extinction curve is that of SMC (Small Magellanic Cloud) and the total-to-selective extinction is taken $R_{\text{V}} = 2.93$. The columns designation is the same as for Table 12 with an addition of the lower photon index (left) and the break energy in eV.

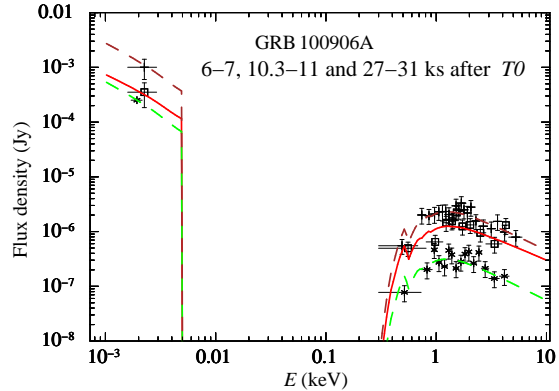
Fit ID	$t - T_0$ (s)	Photon index	E_{break} (eV)	Photon index	$N_{\text{H}}^{\text{int}}$ (10^{22} cm^{-2})	$A_{\text{V}}^{\text{int}}$	χ^2/dof
100906.3	6000 – 7000	1.96 ± 0.05	$0.4^{+0.3}_{-0.2}$	< 0.4	36.6/42
	10500 – 11000	1.9 ± 0.1			
	28000 – 30400	2.01 ± 0.02			
100906.4	45000 – 65000	-1.3 ± 0.7	2.5 ± 0.3	2.34 ± 0.04	$0.25^{+0.55}_{-0.25}$	0.35 ± 0.09	9.78/10

(see table 1 in Racusin et al. (2009), references therein and reviews of Mészáros 2002; Zhang & Mészáros 2004; Piran 2005). Before the break, for the ISM environment and the ‘slow cooling’ regime and using $\beta_{\text{XRT}} = 1.0 \pm 0.3$ we get $\alpha = 3\beta/2 = 1.5 \pm 0.45$ (c.f. $\alpha = 1.68 \pm 0.02$ in Table 14, the 1st row, before the break). The electron spectral index is $p = 2\beta + 1 = 3.0 \pm 0.6$. After the break, applying a uniform spreading jet scenario, we arrive at $\alpha = 2\beta + 1 = 3.2 \pm 0.4$. The electron spectral index has the same functional form $\beta = (p - 1)/2$. The value of β is almost the same, ($\beta_{\text{XRT}} = 1.1 \pm 0.2$), and we arrive at $p = 3.2 \pm 0.4$. Thus the closure relations can be satisfied for a consistent value of p . The relations applied imply that $\nu_{\text{m}} < \nu_{\text{x}} < \nu_{\text{c}}$, where ν_{m} and ν_{c} are the characteristic synchrotron and cooling frequencies, respectively.

We have tried to find out whether this break is achromatic. The OSN data R show that around 52 ks there is an abruptness of the R light curve (the fit parameters in the row 2 of Table 14). But the time sampling of OSN R data alone is not good enough to clear up the behavior around this time. If we combine the OSN and NOT data (the 3rd row in Table 14), we apparently do not get an achromatic peak as the tentative break on the R light curve shifts to about 35 ks.

The slope of the R light curve (OSN+NOT) before the break is obtained by the data, crowded around 30 ks, and might be misleading. If we suggest that the slope of the R light curve before the break equals to the slope of the MASTER light curve for the earlier data (blue crosses in Fig. 11), that is 1.08 (also reported by Kuvshinov et al. 2010), the break time shifts to $39.0^{+0.5}_{-1}$ ks (the temporal slope after the break remains the same ~ 2.2 as in the 4th row of Table 14.).

We conclude that the X-ray data alone indicates a jet break that can satisfy the closure relations. The optical data do not yield confidence about the achromatic character of the break. For the discussion of Amati and Ghirlanda relations, see § 5.4.

**Figure 9.** Spectral distributions of GRB 100906A at three time intervals: 6000–7000, 10500–11000 and 28000–30400 s (points, squares and crosses with bars, respectively). The optical data are: the MASTER $P = 17.54 \pm 0.05$ for 6000–7000 s, $P = 18.7 \pm 0.3$ for 10500–11000 s and OSN $R = 18.70 \pm 0.02$ for 28000–30400 s, additionally corrected for the Galactic extinction $A_{\text{V}} = 1.194$ and $A_{\text{R}} = 0.963$ (NED; Schlegel, Finkbeiner & Davis 1998). Lines show the best-fitting absorbed power laws, whose parameters are listed as Fit 100906.3 in Table 13.

5 DISCUSSION

5.1 Optical emission sites of GRBs 100901A and 100906A

The prompt behavior of the two closely studied GRBs is quite distinct. For GRB 100901A, we see a similarity of light curves in the optical, γ , and X-rays at around 300–500 s after the trigger. For GRB 100906A, such similarity of temporal behaviour is absent. It has a perfectly smooth optical light curve, gradually rising and decaying, a different profile from that in the 15–150 keV band (Fig. 3).

From this point of view, GRBs 100901A and 100906A support the earlier noticed diversification for optical emission detected during the first few minutes after the onset

Table 14. Parameters of the time fits to the GRB 100906A light curves, where slope α is quoted in $F_\nu \propto t^{-\alpha} \nu^{-\beta}$. The first three fits are done with the broken power-laws, and the last one, with the power law. Also given are the spectral indices in the XRT spectral range (β_{XRT}), retrieved from the *Swift* Burst Analyser and averaged over the relevant time intervals. The time intervals are the two parts of the whole time span (2nd column), divided at the break time (5th column).

Light curve	Time (ks)	before break α	$\langle\beta_{\text{XRT}}\rangle$	t_{break} (ks)	after break α	$\langle\beta_{\text{XRT}}\rangle$	χ^2/dof
3 – 10 keV	10 – 300	1.68 ± 0.02	1.0 ± 0.3	51^{+4}_{-3}	$2.9^{+0.1}_{-0.3}$	1.1 ± 0.2	145/78
<i>R</i> (OSN)	28 – 54	1.36 ± 0.05	1.1 ± 0.2	$51.9^{+0.5}_{-0.2}$	10^{+13}_{-3}	...	56.0/55
<i>R</i> (OSN+NOT)	28 – 310	0.14 ± 0.02	1.1 ± 0.2	$34.9^{+0.5}_{-0.2}$	$2.17^{+0.03}_{-0.04}$	1.0 ± 0.2	135/58
1-3 eV (MASTER)	0.18 – 2.52	1.08 ± 0.02	1.3 ± 0.4	13.9/12

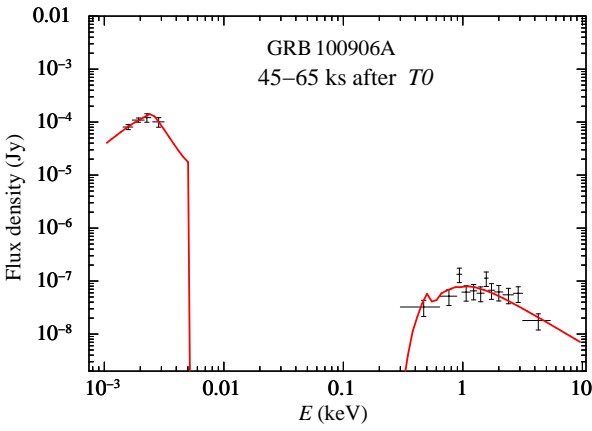


Figure 10. Spectrum of GRB 100906A compiled from the XRT data in the interval 45–65 ks and optical *BVIR* observations obtained by OSN around 14 h after the trigger (in the interval 50.9–54.0 ks) and corrected for the Galactic extinction. Solid line is the best-fitting absorbed broken power law model, whose parameters are listed as Fit 100906.4 in Table 13.

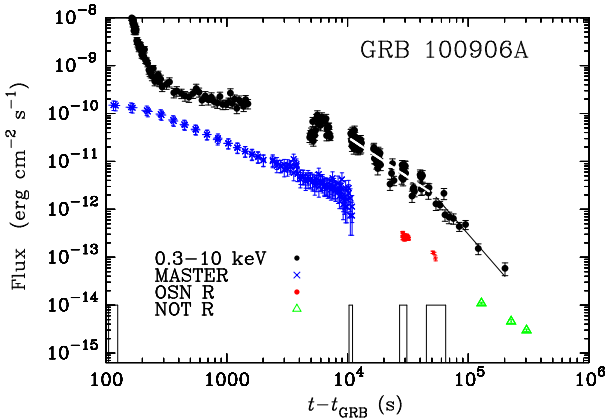


Figure 11. GRB 100906A light curves: unabsorbed 0.3–10 keV flux (black dots) observed by *Swift*/XRT, unfiltered MASTER band flux (blue crosses), *R*-band flux by the OSN (red dots), and *R*-band flux by the NOT (green triangles). The optical points are corrected for the Galactic extinction. Broken-power law fit is plotted over the 0.3–10 keV light curve in white and black color, before and after the break time at 51 ks, respectively. Thin-line rectangles show the time intervals selected for spectral analysis.

of a GRB (e.g., Vestrand et al. 2005, 2006): in some cases the prompt optical flux variations are correlated with the prompt γ -emission, and in other cases early optical afterglow light curve is uncorrelated with the γ -ray light curve.

Such division of GRBs can be understood within the picture of the optical emission generated from different sites of the relativistic jet: in the internal, external forward, or reverse shock waves (e.g., Sari & Piran 1999; Mészáros & Rees 1999). The external forward shocks arise due to the interaction of the ejected material with the ISM and propagate into the ambient media, the reverse shock propagates into the ejecta itself, and the internal shocks are produced because of the collisions among many engine-ejected shells (e.g., Meszaros & Rees 1997; Sari & Piran 1997). The correlation between the optical, γ , and X-rays can be achieved, if the optical emission is produced by the synchrotron mechanism within the same region as the hard radiation.

The early X-ray and soft γ -ray spectrum of GRB 100901A shows a dependence close to $\nu^{-1/2}$ which is typical for the synchrotron radiation if $\nu_c < \nu < \nu_m$ (where ν_m and ν_c are the characteristic synchrotron and cooling frequencies, respectively) in the regime when electrons lose energy very quickly (see, e.g., Sari, Piran & Narayan 1998; Sari & Piran 1999). Adding the MASTER optical point (corrected for the Galaxy extinction), and fitting simultaneously the optical, 0.3 – 10 keV, and 15 – 150 keV data by an absorbed power law, we can determine the magnitude of the optical extinction in the host. Consistent values of A_V^{int} and N_H^{int} are obtained for the prompt spectral distributions (Table 10), indicating a persisting relation between the optical and high energy part of the spectrum. Basically, this means that the optical emission is the low-energetic photons from the same region that generates the high energy photons.

We should add that the data can also be reconciled with the prompt spectral distributions of GRB 100901A peaking between the optical and X-rays, if $\nu_{\text{opt}} < \nu_c < \nu_x$. Then, a migration of the cooling frequency $\nu_c \propto t^{-1/2}$, see, for example, Sari, Piran & Narayan 1998) may be hidden in the errors of resulted A_V^{int} . Spectral fitting of an absorbed power law to the late-time MASTER and 0.3–10 keV data provides $A_V^{\text{int}} = 0.45 \pm 0.15$, lower than $A_V^{\text{int}} = 0.8 \pm 0.1$ for the prompt fits (values are for the SMC type of the extinction law; see § 4.2). This could be a confirmation of the above suggestion, but a detailed discussion is beyond the aims of the present study.

In contrast to the above picture, GRB 100906A exhibits no correlation between the optical and high energy emission

at 15–150 keV. We suggest that in this case the optical radiation originates at the front of the external shock, and the light curve shows a smooth conversion of a bow shock to a self-similar mode of the afterglow with a power decay $F_{\text{opt}} \propto t^{-\alpha}$ with $\alpha = 1.08 \pm 0.01$ (Table 14, see also Kuvshinov et al. 2010).

A critical test for determining the site of the optical emission could be the observation of polarization. If radiation in the internal shock occurs in the ordered magnetic field, some polarization is expected (see, e.g., Steele et al. 2009). This implies that the magnetic field coherence scale is larger than the size of the visible emitting region. Thus, a discovery of a considerable ($> 10\%$) polarization of the optical radiation, correlating with the prompt γ -ray emission, would be a strong evidence in favor of the optical radiation originating in the internal shock. Conversely, the afterglow radiation from the external shock occurs in the chaotic field of the interstellar medium compressed by the shock and should not have a considerable polarization (Gruzinov & Waxman 1999). Low degree of polarization of the optical light would rule out the presence of a large-scale ordered magnetic field in the emitting region (Mundell et al. 2007).

Fig. 4 shows our simultaneous observations of GRB 100906A with two orthogonal polaroids. The signals in the two channels are the same with an accuracy of 0.5 per cent. Absence of the strong polarization is consistent with the picture of the different producing sites of the high-energy and optical radiation in GRB 100906A. However, we should note that the MASTER polarization observations of GRB 100906A were made with two optical tubes of one telescope. Such mode of observations is restricted in the sense of giving definite information on the linear polarization (see the Appendix). Polarization filters are oriented differently in the celestial coordinate system at the telescopes of the MASTER net. A future observation of a suitable GRB by two MASTER telescopes should thus provide an accurate polarization information. For the observations of GRB 100906A, we can infer that in the time interval from 100 s to ~ 1 h the degree of linear polarization of the optical emission is less than 10% with probability of about 60 per cent (see the Appendix and Fig. 14). The full information of the inferred fractional linear polarization can be retrieved from Fig. 14. We note that the probabilities are obtained under a very conservative assumption that a source can have any fractional linear polarization from 0 to 100%.

5.2 General spectral properties

In order to view spectral characteristics of the observed GRBs at one glance, we construct in Fig. 12 a diagram of the optical flux density versus X-ray flux density at 3 keV, following Jakobsson et al. (2004). However, we plot not the values extrapolated to 11 h time mark, but rather the evolution for each GRB. Here, a spectral index β ($F_\nu \propto \nu^{-\beta}$) is shown by straight lines. Each optical observation is corrected for the Galactic extinction at a specific waveband using the NED Galactic Extinction calculator. As the intrinsic spectrum is not known a-priori, we do not include a correction for the host extinction. The 3 keV flux densities are the best-fitting values obtained with an absorbed power law model in

the XRT/*Swift* energy band. For GRBs 100902A, 100905A, and 101020A, only upper optical limits are shown.

The limit for GRB 100902A at 132 – 162 s yields that the burst was rather X-ray bright and very faint in the optical waveband at the time, possibly due to a large intrinsic extinction. Provided that $T_{90} = 429$ s (Stamatikos et al. 2010), one can expect that the GRB would have low β_{ox} at $(0.3 - 0.4) T_{90}$. It might be a ‘dark’ GRB according to classification by Jakobsson et al. (2004), bearing in mind its very prominent position on the diagram. GRB 100902A appears to be darker than any of the GRBs of the sample of Jakobsson et al. (2004, see their Fig. 1), with all of them being above the $\beta_{\text{ox}} = 0$ line.

An anti-correlation between excess absorption column densities and redshifts of GRBs is expected due to the shift of the source rest-frame energy range below 1 keV out of the X-Ray Telescope observable energy range. Thus Grupe et al. (2007) suggest a relation to estimate an upper limit on the redshift. From the late-time spectrum of GRB 100902A, one finds an excess absorption column density of $\sim 2.8^{+0.6}_{-0.7} \times 10^{21} \text{ cm}^{-2}$ and upper limit for $z \approx 3.2$ (substituting lower value of N_{H} from expression (1) of Grupe et al. (2007)). High redshifts are thought to be possibly responsible for darkness of GRBs, but the redshift obtained above is not high enough for this scenario (see, e.g., Jakobsson et al. 2004, and references therein); on the other hand, expression by Grupe et al. (2007) is inferred for non-dark GRBs and might be unapplicable. We also note that analysis of Campana et al. (2010) who use a cutoff power-law model suggest a higher redshift, $z \sim 4.5$.

The MASTER observation of GRB 100905A was done at the time interval 150–180 s that is much later than its $T_{90} = 3.4$ s. It can belong to the class of intermediate duration GRBs (Horváth 1998, 2002; Mukherjee et al. 1998). At 150–180 s after the trigger its XRT spectral slope is $\beta_x = 0.2 \pm 0.2$. If the optical emission belong to the same spectral distribution, it would explain its weakness, because the line $\beta_{\text{ox}} = 0.2$ intersects the region of the 100905A on the diagram at the F_{opt} values well below the optical limit.

GRB 101020A could not be observed by *Swift*/XRT. The flux density at 3 keV for time $0.65 \times T_{90}$, where $T_{90} = 177$ s, is extrapolated from the BAT data and has a considerable uncertainty, thus resulting in a wide area in Fig. 12. Nevertheless, the optical-to-X-ray flux ratio can be similar to that of GRBs 100901A and 100906A.

We see from Fig. 12 that the flux density ratios of GRB 100901A and GRB 100906A ultimately tend to the area between $\beta = 0.5$ and 1.25. This is consistent with the fireball model (e.g. Sari, Piran & Narayan 1998). Spectral slope ~ -1 at late times is consistent with the prediction for the slow-cooling regime for frequencies higher than the cooling frequency for electrons with distribution of Lorentz factors $N(\gamma_e) \propto \gamma_e^{-p}$ with $p \gtrsim 2$.

The distinct prompt behavior of GRB 100901A and GRB 100906A is evident in the diagram. We witness the optical and X-ray flux density correlation in GRB 100901A at the time of the last γ -ray pulse, together with an approximately constant spectral index. In GRB 100906A, during the γ -ray pulse, occurring about 100 s after the trigger, the 3 keV flux density undergoes a strong variation. The same can be said about the spectral indices in the XRT and BAT bands. However, the optical flux density is roughly at

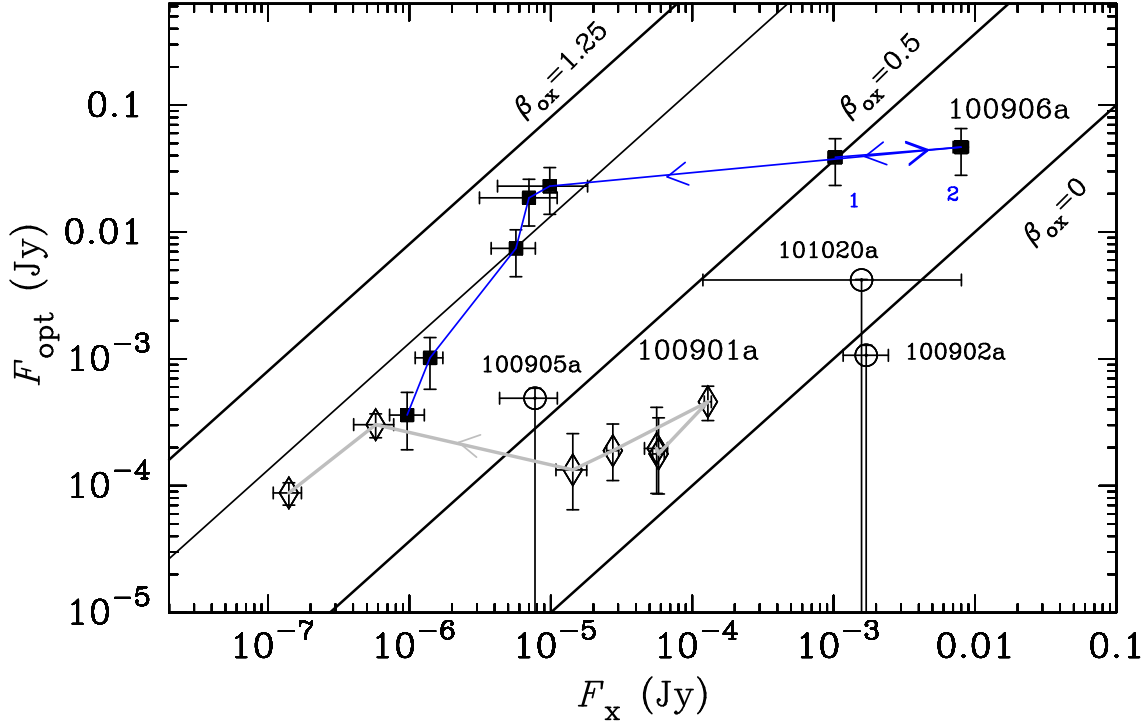


Figure 12. Diagram of the optical flux density versus X-ray flux density at 3 keV for five GRBs observed by MASTER in September and October 2010. Each point represents a simultaneous observation in the optical and by *Swift*/XRT. The optical flux densities have been corrected for the Galactic extinction. Diamonds connected with grey line show evolution of GRB 100901A (eight time intervals: 193–233, 312–372, 387–467, 481–581, 595–715, 3800–4150, 27000–28500, and 102800–121500 s); squares connected by blue lines, of GRB 100906A (seven time intervals: 84–94 (point 1), 105–125 (point 2), 330–390, 410–480, 942–1112, 6000–7000, and 10300–11000 s). For GRBs 100902A, 100905A, and 101020A, only upper limits on optical flux density are given at post-trigger times 132–162, 150–180, and 106–126 s, respectively. When tracks are parallel to $\beta = \text{const}$ lines, the optical flux density is emphatically correlated with the 3 keV flux density. We adopt Galactic extinctions $A_V = 1.037$ for GRB 100902A, $A_V = 0.191$ for GRB 100905A, and $A_V = 0.051$ for GRB 101020A from the NED Extragalactic Calculator.

the same level. We remind that the spectral fitting provides an evidence that the prompt high energy SED has a peak, which migrates from about 30 to 4 keV at times 80–130 s after T_0 (see § 4.1). It should be added that during those times the X-ray emission in the interval of 0.3–10 keV can be contributed by the two different sites with a proportion varying with time: the one that is responsible for the γ -rays and one producing the optical photons.

5.3 Amati and Ghirlanda relations for GRB 100901A

The total duration BAT spectrum of GRB 100901A yields $E_{\text{iso}} = 6.3 \times 10^{52}$ erg in the energy interval 1 – 10^4 keV in the rest frame. From the Amati relation (Amati 2006) one gets the expected position of the energy distribution peak in the rest frame $E_{p,i} = 230$ keV, which translated to the observer frame becomes $E_p \sim 100$ keV. This does not contradict with the lower limit $E_p^{\text{min}} \sim 75$ keV, derived on the basis that no characteristic energy can be found from the spectral analysis of the BAT data, and the photon index of the power law is about -1.5.

The 0.3–10 keV light curve $\propto t^{-1.5}$ from 4×10^4 s to about 10^6 s when a possible steepening occurs. The MASTER *W*-band light curve enables only a rough evaluation of temporal index in the interval $3 \times 10^4 - 3 \times 10^5$ s: it is

decaying approximately as $\sim t^{-1.3}$ with just one late optical point at $\sim 10^5$ s. Using the tentative jet break time $\sim 10^6$ s, one gets the opening half-angle of the jet ~ 13 deg for efficiency of converting the ejecta energy into γ -rays $\eta_\gamma = 0.2$ and the number density of the ambient medium $n = 3 \text{ cm}^3$. Few jets are reported to have comparably wide angles (Ghirlanda, Ghisellini & Lazzati 2004). Corresponding collimation-corrected energy would be $E_\gamma = 1.7 \times 10^{51}$ erg, which using Ghirlanda relation predicts $E_{p,i} \sim 700$ keV, a value about 3 times higher than prediction of the Amati relation.

We conclude that GRB 100901 can be consistent with the Amati relation, if $E_{p,i} \sim 230$ keV, but the Ghirlanda relation is hardly applicable.

5.4 Amati and Ghirlanda relations for GRB 100906A

Golenetskii et al. (2010), fitting the spectrum of GRB 100906A in the time interval 3 – 142 s with the Band function, derive values $E_{\text{peak}} = 142^{+119}_{-60}$ keV and $E_{\text{iso}} = (2.2 \pm 0.4) \times 10^{53}$ erg. The peak of the energy distribution in the rest frame is at $E_{p,i} = (1 + z) \times E_{\text{peak}} = 387^{+324}_{-164}$ keV. Central values of E_{iso} and $E_{p,i}$ are close to the Amati correlation $E_{p,i} = 95 \times E_{\text{iso}}^{0.49}$ (figure 2 of Amati 2006).

If we assume jet break time $t_b = 51 \pm 4$ ks (see § 4.4) and substitute the above E_{iso} into equation (1) of Ghirlanda, Ghisellini & Lazzati (2004) (where we assume the values of the efficiency of converting the ejecta energy into γ -rays $\eta_\gamma = 0.2$ and the number density of the ambient medium $n = 3 \text{ cm}^2$), we obtain the opening half angle of the jet $\theta_j = 3.31 \pm 0.08$ deg. Then the collimation-corrected energy is $E_\gamma \sim (3.7 \pm 0.7) \times 10^{50}$ erg. The last value together with $E_{p,i}$ agree with the Ghirlanda relation $E_{p,i} \simeq 480(E_\gamma/10^{51} \text{ erg})^{0.7}$ (figure 1 of Ghirlanda, Ghisellini & Lazzati 2004). This is especially so due to the big uncertainty in the observed E_{peak} value of GRB 100906A.

5.5 Long life of a central engine

A prolonged activity of the central engine was suggested as a source of an extended afterglow by Katz & Piran (1997). It was considered later as an explanation for plateaus on X-ray light curves of some GRBs (e.g., Zhang & Mészáros 2001; Zhang et al. 2006; Liang, Zhang & Zhang 2007; Willingale et al. 2007; Lipunov & Gorbovskey 2008). In particular, sharp drops at late times on the light curves indicate that such variations are likely due to some internal mechanisms (Troja et al. 2007; Zhang 2009). To account for a lasting activity of the central engine of GRBs, a model of a rapidly-spinning, highly-magnetized neutron star, a ‘proto-magnetar’, formed in the result of a core collapse, was proposed (see review by Metzger 2010). Another object that can provide a long-term energy supply is a rapidly-spinning, magnetized collapsed core with mass exceeding an upper limit for a neutron star. Its fast rotation stops the collapse, and a quasi-stationary configuration is presumably formed at this stage, which is called a ‘spinar’ (Lipunova 1997; Lipunov & Gorbovskey 2007). Before a collapse to a black hole is possible, enough angular momentum should be taken out from the system. The time required for angular momentum dissipation determines the duration of the central engine activity and depends on the magnetic field strength, as the energy and angular momentum losses are governed by the magneto-dipole mechanism.

Lipunov & Gorbovskey (2008) proposed a set of 1-D equations determining evolution of a collapsing rotating magnetized core with main relativistic effects taken into account. These equations describe the principal behavior of both the proto-magnetar and the spinar. Solutions suggest two peaks in energy release: the first takes place when dynamical collapse is halted by centrifugal or pressure forces, and the second, when final contraction occurs. The peaks are separated by a plateau. Three exemplary solutions of equations by Lipunov & Gorbovskey (2008) are shown in Fig. 13. The first peak is set to occur at zero time and not shown in detail. In the model, the first peak is evaluated on a dynamical time-scale and does not involve specific jet and afterglow radiation mechanisms. If the first stage of a collapse finishes close to $r_g = GM/c^2$, then the second peak is extinguished. A power of a proto-magnetar, defined by the pulsar dipole mechanism, approaches the t^{-2} law after the second peak. A power of a spinar has always a very sharp drop after the second peak. For each of the models in Fig. 13, calculated power is multiplied by an arbitrary factor of 0.1.

Two curves with lower plateaus represent models with

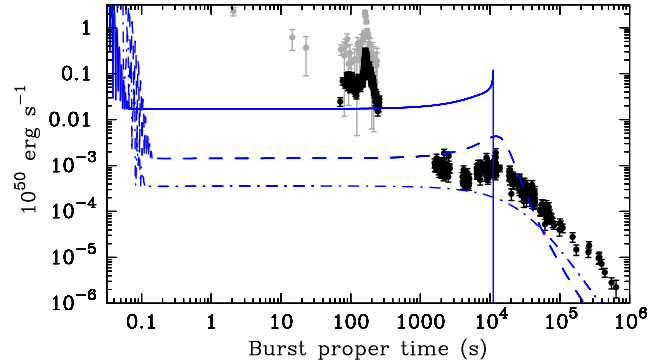


Figure 13. Energy release of a collapsing core calculated following Lipunov & Gorbovskey (2008). Points with bars are the observed 0.3–10 keV and 15–150 keV flux from GRB 100901A (Sakamoto et al. 2010b; Page & Immler 2010) translated to redshift 1.408. Three curves with plateaus represent numerical solutions for energy release rates, multiplied by 0.1, for cores of different mass and angular momentum. The dashed and dot-dashed lines are solutions for proto-magnetars of the same mass and with different angular momentum at the halt of the initial dynamical collapse that produced the first peak before the plateau. The first peak is referred to time zero; the details of the first peak are of no relevance. The top solid line shows a solution for a collapsing core with such a mass that makes a collapse to a black hole inevitable. For specific parameters of the models, see Discussion.

mass $M = 1.9 M_\odot$. They both go as $\propto t^{-2}$ at late times. In the model with monotonic transition to a decay, a proto-magnetar forms with period $P = 2$ ms and poloidal magnetic field $B \sim 4 \times 10^{14}$ G at $\sim 13 r_g$. The middle plateau represents a newly born magnetar of higher angular momentum: the dynamical collapse halts at about $40 r_g$ with $P = 5$ ms and $B \sim 7 \times 10^{13}$ G. The object contracts further, to $10 r_g$, causing a spin up to $P = 1.7$ ms and the dipole magnetic field amplification up to $\sim 10^{15}$ G. This specific evolution manifests itself as a bump at the end of the plateau. The solid curve shows a solution for a spinar with $M = 4 M_\odot$. At the plateau, the dimensionless Kerr parameter $a_{\text{Kerr}} = Jc/GM^2 = 3$, $P \sim 1$ ms, $B \sim 1.5 \times 10^{13}$ G, and the characteristic radius $15 r_g$. The spike at the end is numerically solved and indicates the collapse to a black hole. The initial magnetic field strengths are chosen in order to obtain the characteristic time of a plateau $\sim 10^4$ s.

A spinar and a proto-magnetar, both can explain long activity of GRBs. The law of temporal decay after the second peak (or the end of a plateau) can be defined by an afterglow and does not allow us to decide which compact object is behind the scene. The efficiency factor, which is set 0.1 for Fig. 13, cannot be constrained in our general approach.

6 SUMMARY

The net of optical robotic telescopes MASTER coming into full operation over the Russia territory is encouraged by the need of dense early observations of GRBs around the globe. Optical ground-based observations, with polarization measurements, are indispensable in revealing the nature of the GRB central engine. The MASTER team is working on obtaining optical linear polarization information at the earliest time since a GRB trigger, before γ -emission ceases, by ob-

serving simultaneously with several telescopes. Our goal is to deliver full polarization information for GRBs in the optical band as early as possible after the trigger time.

Here we presented the early results of the MASTER network. During 2010, MASTER observed five GRBs described in this paper. Optical transients were found for two bursts: GRBs 100901A and GRB 100906A. Their detailed analysis was done basing on the MASTER data, the data from the 1.5-m telescope at Sierra Nevada Observatory and 2.56-m Nordic Optical Telescope, as well as the publicly available data from the *Swift* mission.

The light curves and spectra of GRBs 100901A and 100906A suggest different origin of the prompt optical emission. The correlation between the optical and high-energy light curves of GRB 100901A, as well as the results of spectral fitting favor the hypothesis of the common origin for the optical and high-energy spectrum. During the γ -ray flare started at about 300 s after the trigger, the slope of the spectral distribution from the optical to 150 keV is close to $-1/2$. This is expected for the synchrotron radiation at the frequencies above the cooling and below the characteristic synchrotron frequency in the ‘fast cooling’ regime (see, e.g. Sari & Piran 1999). The resulted values of the host optical extinction are consistent for the prompt fits and similar to the values obtained by fitting an absorbed power law to the late-time spectral data. This means that the prompt optical points lie on the same spectral distribution which describes the γ - and X-ray data, supporting the hypothesis of their common production site and mechanism. The estimated ratio of the GRB host hydrogen column density $N_{\text{H}}^{\text{int}}$ to the total extinction $A_{\text{V}}^{\text{int}}$ suggests that the host of GRB 100901A possesses the metal-to-dust ratio comparable to the level measured for the Milky Way or Magellanic Clouds.

In GRB 100906A, no apparent correlation between the optical and 15–150 keV light curves is seen. We suggest that in GRB 100906A the prompt optical radiation originates in a region different from the γ -ray production site, probably, in a front shock. An analysis of GRB 100906A reveals that a spectral component, responsible for the γ -ray pulse at ~ 100 s after the trigger and the downward migration of the X-ray peak on the spectral energy distribution, does not correlate with the optical emission at these times.

Signals in two orthogonal polarizations, measured by the MASTER telescope at Tunka from GRB 100906A, are found to be equal within 0.5 per cent. We calculate the probability distribution for the fractional linear optical polarization of GRB 100906A. We point out that a future observation of a GRB by at least two MASTER telescopes should yield an accurate polarization information.

The 0.3–10 keV light curve of GRB 100906A has a break at around 14 hr after the trigger. The X-ray spectral index (non-variable around the break) and the temporal slopes can be reconciled with the closure relations for the relativistic jet in the ‘slow cooling’ regime before the break and the spreading uniform jet after the break. It is not clear from the data in the R band if this break is achromatic. Estimated jet opening angle, 3.31 ± 0.08 degrees, and collimation-corrected energy, $E_{\gamma} \sim (3.7 \pm 0.7) \times 10^{50}$ erg, imply that GRB 100906A follows the Amati relation and does not contradict the Ghirlanda relation. An analysis of the late-time spectra provides the upper limit on the optical extinction in the GRB host.

ACKNOWLEDGMENTS

We thank the referee for many useful comments. We are grateful to T. Piran for his help. We also thank K. Sokolovsky. We acknowledge Taka Sakamoto and Scott D. Barthelmy for the BAT data. This work was supported by the Ministry of Science of the Russian Federation (state contract no. 02.740.11.0249). E.S.G. thanks the Foundation for Non-Profit Programs ‘Dynasty’. The research of J.G., A.J.C.T., J.C.T., M.J., and R.S.R. is supported by the Spanish programs AYA2007-63677, AYA2008-03467/ESP and AYA2009-14000-C03-01. Authors are grateful to S.M. Bodrov for the ceaseless support of the MASTER-Net. This work made use of data supplied by the UK *Swift* Science Data Centre at the University of Leicester. This research has made use of the NASA/IPAC Extragalactic Database (NED) which is operated by the Jet Propulsion Laboratory, California Institute of Technology, under contract with the National Aeronautics and Space Administration. We used the publicly available results of the Sloan Digital Sky Survey, whose web site is <http://www.sdss.org/>. This research has made use of NASA’s Astrophysics Data System.

REFERENCES

- Abazajian K. N. et al., 2009, *ApJS*, 182, 543
- Akerlof C. et al., 2000, *ApJ*, 532, L25
- Amati L., 2006, *MNRAS*, 372, 233
- Arnaud K. A., 1996, in *Astronomical Society of the Pacific Conference Series*, Vol. 101, *Astronomical Data Analysis Software and Systems V*, G. H. Jacoby & J. Barnes, ed., pp. 17–20
- Atwood W. B. et al., 2009, *ApJ*, 697, 1071
- Barthelmy S. D. et al., 2010a, *GRB Coordinates Network, Circular Service*, 11218, 1 (2010), 1218, 1
- , 2010b, *GRB Coordinates Network, Circular Service*, 11233, 1 (2010), 1233, 1
- Beardmore A. P., Markwardt C. B., 2010, *GRB Coordinates Network, Circular Service*, 11244, 1 (2010), 1244, 1
- Butler N. R., Kocevski D., 2007, *ApJ*, 663, 407
- Campana S., Starling R. L. C., Evans P. A., Sakamoto T., 2010, *GRB Coordinates Network, Circular Service*, 11195, 1 (2010), 1195, 1
- Chornock R., Berger E., Fox D., Levan A. J., Tanvir N. R., Wiersema K., 2010, *GRB Coordinates Network, Circular Service*, 11164, 1 (2010), 1164, 1
- de Ugarte Postigo A. et al., 2011, *A&A*, 525, A109
- Evans P. A. et al., 2009, *MNRAS*, 397, 1177
- , 2010, *A&A*, 519, A102
- Everett M. E., Howell S. B., 2001, *PASP*, 113, 1428
- Gehrels N. et al., 2004, *ApJ*, 611, 1005
- Ghirlanda G., Ghisellini G., Lazzati D., 2004, *ApJ*, 616, 331
- Golenetskii S. et al., 2010, *GRB Coordinates Network, Circular Service*, 11251, 1 (2010), 1251, 1
- Gorbovskoy E. et al., 2010, *GRB Coordinates Network, Circular Service*, 1185
- Grupe D., Nousek J. A., vanden Berk D. E., Roming P. W. A., Burrows D. N., Godet O., Osborne J., Gehrels N., 2007, *AJ*, 133, 2216

- Gruzinov A., Waxman E., 1999, *ApJ*, 511, 852
- Hayes D. S., 1985, in *IAU Symposium*, Vol. 111, Calibration of Fundamental Stellar Quantities, D. S. Hayes, L. E. Pasinetti, & A. G. D. Philip, ed., pp. 225–249
- Horváth I., 1998, *ApJ*, 508, 757
- , 2002, *A&A*, 392, 791
- Immler S. et al., 2010, GRB Coordinates Network, Circular Service, 11159, 1 (2010), 1159, 1
- Ivanov K. et al., 2010a, GRB Coordinates Network, Circular Service, 11161, 1 (2010), 1161, 1
- , 2010b, GRB Coordinates Network, Circular Service, 11163, 1 (2010), 1163, 1
- , 2010c, GRB Coordinates Network, Circular Service, 11216, 1 (2010), 1216, 1
- Jakobsson P., Hjorth J., Fynbo J. P. U., Watson D., Pedersen K., Björnsson G., Gorosabel J., 2004, *ApJ*, 617, L21
- Jensen B. L. et al., 2001, *A&A*, 370, 909
- Kalberla P. M. W., Burton W. B., Hartmann D., Arnal E. M., Bajaja E., Morras R., Pöppel W. G. L., 2005, *A&A*, 440, 775
- Katz J. I., Piran T., 1997, *ApJ*, 490, 772
- Kornilov V. G. et al., 2011, *Experimental Astronomy*, accepted for publication
- Krushinski V. et al., 2010a, GRB Coordinates Network, Circular Service, 11182, 1 (2010), 1182, 1
- , 2010b, GRB Coordinates Network, Circular Service, 11359, 1 (2010), 1359, 1
- , 2010c, GRB Coordinates Network, Circular Service, 11361, 1 (2010), 1361, 1
- Kulkarni S. R. et al., 1998, *Nature*, 395, 663
- Kuvshinov D. et al., 2010, GRB Coordinates Network, Circular Service, 11235, 1 (2010), 1235, 1
- Landi Degl’Innocenti E., Bagnulo S., Fossati L., 2007, in *Astronomical Society of the Pacific Conference Series*, Vol. 364, The Future of Photometric, Spectrophotometric and Polarimetric Standardization, C. Sterken, ed., pp. 495–502
- Liang E.-W., Zhang B.-B., Zhang B., 2007, *ApJ*, 670, 565
- Lipunov V., Gorbvskoy E., 2007, *ApJ*, 665, L97
- Lipunov V. et al., 2010, *Advances in Astronomy*, article id. 349171
- Lipunov V. M., Gorbvskoy E. S., 2008, *MNRAS*, 383, 1397
- Lipunova G. V., 1997, *Astronomy Letters*, 23, 84
- Markwardt C. B. et al., 2010, GRB Coordinates Network, Circular Service, 11227, 1 (2010), 1227, 1
- Marshall F. E. et al., 2010, GRB Coordinates Network, Circular Service, 11214, 1 (2010), 1214, 1
- Mészáros P., 2002, *ARA&A*, 40, 137
- Mészáros P., Rees M. J., 1997, *ApJ*, 476, 232
- Mészáros P., Rees M. J., 1999, *MNRAS*, 306, L39
- Metzger B. D., 2010, in *Astronomical Society of the Pacific Conference Series*, Vol. 432, New Horizons in Astronomy: Frank N. Bash Symposium 2009, L. M. Stanford, J. D. Green, L. Hao, & Y. Mao, ed., pp. 82–96
- Mukherjee S., Feigelson E. D., Jogesh Babu G., Murtagh F., Fraley C., Raftery A., 1998, *ApJ*, 508, 314
- Mundell C. G. et al., 2007, *Science*, 315, 1822
- Page K. L., Immler S., 2010, GRB Coordinates Network, Circular Service, 11171, 1 (2010), 1171, 1
- Pei Y. C., 1992, *ApJ*, 395, 130
- Pickles A., Depagne É., 2010, *PASP*, 122, 1437
- Piran T., 2005, *Reviews of Modern Physics*, 76, 1143
- Racusin J. L. et al., 2009, *ApJ*, 698, 43
- Sakamoto T. et al., 2010a, GRB Coordinates Network, Circular Service, 11358, 1 (2010), 1358, 1
- , 2010b, GRB Coordinates Network, Circular Service, 11169, 1 (2010), 1169, 1
- Sakamoto T., Baumgartner W. H., Beardmore A. P., Cummings J. R., Evans P. A., Gehrels N., Gelbord J. M., et al., 2010c, GRB Coordinates Network, Circular Service, 11181, 1 (2010), 1181, 1
- Sanchez-Ramirez R., Tello J. C., Sota A., Gorosabel J., Castro-Tirado A. J., 2010, GRB Coordinates Network, Circular Service, 11180, 1 (2010), 1180, 1
- Sari R., Piran T., 1997, *ApJ*, 485, 270
- , 1999, *ApJ*, 520, 641
- Sari R., Piran T., Narayan R., 1998, *ApJ*, 497, L17
- Saxton C. J. et al., 2010, GRB Coordinates Network, Circular Service, 11357, 1 (2010), 1357, 1
- Schady P. et al., 2010, *MNRAS*, 401, 2773
- Schlegel D. J., Finkbeiner D. P., Davis M., 1998, *ApJ*, 500, 525
- Siegel M. H., Marshall F. E., 2010, GRB Coordinates Network, Circular Service, 11237, 1 (2010), 1237, 1
- Sota A., de Ugarte Postigo A., Castro-Tirado A. J., 2010, GRB Coordinates Network, Circular Service, 11220, 1 (2010), 1220, 1
- Stamatikos M. et al., 2010, GRB Coordinates Network, Circular Service, 11202, 1 (2010), 1202, 1
- Steele I. A., Mundell C. G., Smith R. J., Kobayashi S., Guidorzi C., 2009, *Nature*, 462, 767
- Tanvir N. R., Wiersema K., Levan A. J., 2010, GRB Coordinates Network, Circular Service, 11230, 1 (2010), 1230, 1
- Tello J. C., Sanchez-Ramirez R., Sota A., Gorosabel J., Castro-Tirado A. J., 2010, GRB Coordinates Network, Circular Service, 11196, 1 (2010), 1196, 1
- Tody D., 1993, in *Astronomical Society of the Pacific Conference Series*, Vol. 52, Astronomical Data Analysis Software and Systems II, R. J. Hanisch, R. J. V. Brissenden, & J. Barnes, ed., pp. 173–183
- Troja E. et al., 2007, *ApJ*, 665, 599
- Vestrand W. T. et al., 2005, *Nature*, 435, 178
- , 2006, *Nature*, 442, 172
- Willingale R. et al., 2007, *ApJ*, 662, 1093
- Winkler C. et al., 2003, *A&A*, 411, L1
- Zhang B., Fan Y. Z., Dyks J., Kobayashi S., Mészáros P., Burrows D. N., Nousek J. A., Gehrels N., 2006, *ApJ*, 642, 354
- Zhang B., Mészáros P., 2001, *ApJ*, 552, L35
- , 2004, *International Journal of Modern Physics A*, 19, 2385
- Zhang X.-H., 2009, *Research in Astronomy and Astrophysics*, 9, 213

Appendix. Estimating degree of linear polarization from observations with two fixed polarizing filters

Observations of bright GRB 100906 have been made with just one telescope able to provide polarization measurements (the MASTER telescope at Tunka). Generally, if an observation is made only with two polarizing filters at a single set of positions, one can obtain just an estimate on the degree of linear polarization.

In the consideration below we assume zero circular

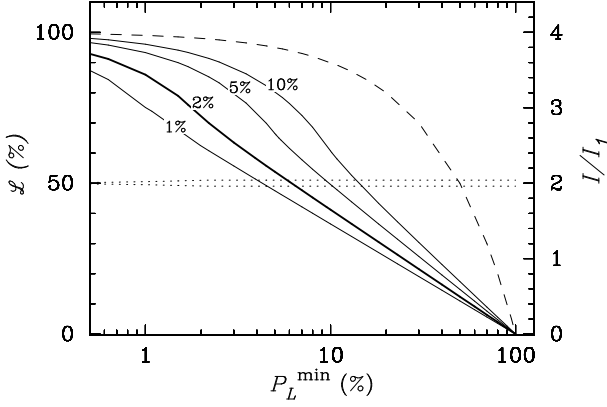


Figure 14. Left axis: likelihood $\mathcal{L}(P_L \geq P_L^{\min} | I_1 \approx I_2)$, where $I_{1,2}$ are the signals from two orthogonal polarizing filters, P_L is an unknown fractional linear polarization of a source, and P_L^{\min} is a value plotted along the x -axis. The several likelihood functions are plotted as solid curves marked with the values of σ_p , the known relative error between the measurements with two orthogonal polarizing filters. The dashed line shows the probability of an unobserved source to have $P_L \geq P_L^{\min}$ under the prior hypothesis that a source has no preference to any degree of linear polarization. Right axis: the ratio of the total intensity I to the measured signal I_1 for $|D| < \sigma_p = 2\%$. Its limits are shown by the double dotted line.

polarization. Let P_L be the fraction of linearly polarized radiation and θ is the angle of maximum polarization, i.e. the angle between the x -axis of the reference system and a segment which a polarization ellipse degenerates into for the case with zero circular polarization (see, e.g., Landi Degl’Innocenti, Bagnulo & Fossati (2007)). Then $P_L = \sqrt{P_Q^2 + P_U^2}$, where $P_Q = Q/I$, $P_U = U/I$, and I , Q , U are the first three Stokes parameters; I is the total intensity with no polarization filter interposed (in this section we do not consider color filters).

To derive value of P_L one needs to perform observations with filters for linear polarization positioned at three angles, for example, at 0° , 45° , and 90° with respect to the reference direction. We have two orthogonal filters at each of the MASTER-II telescopes; thus, if such telescope observes alone, only a lower limit on P_L can be deduced. If this lower limit is a virtual zero, there is still some probability that actual linear polarization is substantial.

Let I_1 and I_2 be the signals of the detector with filters at 0° and 90° interposed. Then a value $D = (I_1 - I_2)/(I_1 + I_2)$ can be calculated, which is expressed as follows:

$$D = P_L \cos 2\theta. \quad (1)$$

If the value of D differs from zero ($|D|$ is greater than the relative error σ_p between measurements with two differently positioned filters), a certain amount of linear polarization is present in the light with a lower estimate for it: $P_L^{\min} = |D|$, calculated as if a filter is interposed at angle 0° or 90° with respect to the direction of polarization plane of the incident light.

If the module of D is less than σ_p , then formally we have zero as a minimum estimate for the degree of linear polarization. 100-percent linear polarization is also possible in this case, if a filter is accidentally positioned so that a source’s polarization plane is inclined by 45° to it. This

possibility can be numerically evaluated considering a total range of the filter positions that would result in a value of $|D| < \sigma_p$. Substituting $D = \sigma_p$ and $\theta = \pi/4 + \delta\theta/2$ in eq. (1), for any preset value of P_L we get a value of the allowable interval $\delta\theta$. As our configuration consists of two orthogonal filters, source polarization plane should be in either of four intervals $\delta\theta$ around angles $N \times \pi/4$, where $N = 1, 2, 3, 4$. Thus, a source with linear polarization degree P_L yields value $|D| < \sigma_p$ with probability $4\delta\theta/2\pi$. Now we can calculate the conditional probability of a source with observed $|D| < \sigma_p$ to have a particular degree of linear polarization P_L using the Bayes’ theorem. We make a conservative assumption that a source can have any fractional linear polarization from 0 to 100%. From this, the likelihood function $\mathcal{L}(P_L > P_L^{\min} | I_1 \approx I_2) = \mathcal{L}(P_L > P_L^{\min} | |D| < \sigma_p)$ can be derived, where $I_1 \approx I_2$ is a realized event, P_L is the actual fractional linear polarization of a source, and P_L^{\min} is some value of it. The probability that the actual linear polarization of a source exceeds value P_L is shown in Fig. 14. Thus, for example, if no difference between I_1 and I_2 is registered in the measurements with 2 per cent error, there is a fifty-percent chance that a source has linear degree of polarization greater than ≈ 6 per cent.

Accordingly, a total intensity from the source is greater than observed $I_1 \approx I_2$. One can see from Fig. 14 that in the observations with $|D| < \sigma_p$ the total intensity is always about the same factor greater (twice) than measured I_1 . This can be seen considering expression for the signal from one polarizer: $I_1 = I(1 - P_L)/2 + I P_L \cos^2 \theta$. For small P_L the light behaves as unpolarized, and for large P_L the allowable interval $\delta\theta$ approaches zero and $\theta \approx \pi/4$.